remote sensing

MDPI

Article

Detection of Archaeological Residues in Vegetated Areas Using Satellite Synthetic Aperture Radar

Christopher Stewart

Department of Civil Engineering and Computer Science, Tor Vergata University of Rome, 00133 Rome, Italy; stewartchrisroma@gmail.com; Tel.: +39-340-624-0484

Academic Editors: Rosa Lasaponara, Clement Atzberger and Prasad S. Thenkabail
Received: 3 November 2016; Accepted: 22 January 2017; Published: 30 January 2017

Abstract: Buried archaeological structures, such as earthworks and buildings, often leave traces at the surface by altering the properties of overlying material, such as soil and vegetation. These traces may be better visible from a remote perspective than on the surface. Active and passive airborne and spaceborne sensors acquiring imagery from the ultraviolet to infrared have been shown to reveal these archaeological residues following the application of various processing techniques. While the active microwave region of the spectrum, in the form of Synthetic Aperture Radar (SAR) has been used for archaeological prospection, particularly in desert regions, it has yet to be fully exploited to detect buried structures indirectly though proxy indicators in overlying materials in vegetated areas. Studies so far have tended to focus on the intensity of the SAR signal, without making full use of the phase. This paper demonstrates that SAR backscatter intensity, coherence and interferometry can be used to identify archaeological residues over a number of areas in the vicinity of Rome, Italy. SAR imagery from the COnstellation of small Satellites for the Mediterranean basin Observation (COSMO-SkyMed) have been obtained for the analysis: 77 scenes in Stripmap and 27 in Spotlight mode. Processing included multitemporal speckle filtering, coherence generation and Digital Elevation Model (DEM) creation from Small Baseline Subsets (SBAS). Comparison of these datasets with archaeological, geological, soil, vegetation and meteorological data reveal that several products derived from SAR data can expose various types of archaeological residues under different environmental conditions.

Keywords: Synthetic Aperture Radar; SAR; archaeology; COSMO-SkyMed; prospection; SAR coherence; SAR intensity; InSAR; SBAS DEM; Rome

---

1. Introduction

1.1. Archaeological Residues

Buried archaeological structures often leave traces on the surface by altering the properties of overlying material [1–5]. Such archaeological structures could include pits, post-holes, ditches and other earthworks, or constructions erected using building material (e.g., brick, stone and mortar). Under certain conditions, these structures may modify overlying material, such as soil, any vegetation growing in the soil [1,3,5], and may even effect the presence of snow and frost covering vegetated or bare soil [2]. Buried archaeological structures may also leave surface topographic traces.

When such buried features sufficiently change the overlying soil to enable their detection they are referred to as soil marks (see Figure 1). These are commonly formed when ploughing activity extracts and upends the topsoil at a sufficient depth to reveal traces of the underlying soil infilling archaeological structures. This underlying soil may differ in its chemical properties, or in the amount and nature of organic matter and anthrosols contained within it [1–3]. Ploughing action may also bring up fragments of constructions and man-made artifacts buried beneath the topsoil, and thus alter the appearance of the soil [6].

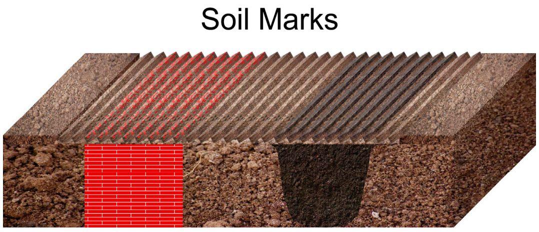

Figure 1. Soil marks: surface residues in bare soil of a buried wall (**left**) and a buried ditch (**right**).

A manifestation of a buried archaeological structure in overlying vegetation is referred to as a crop mark (see Figure 2). Crop marks often emerge as areas of stunted growth (negative crop marks) or more abundant growth (positive crop marks), caused by underlying structures altering the depth and composition of soil in the rooting zone [1,5]. Drought can often enhance such differential vegetation growth, or reveal crop marks over archaeological structures buried at greater depths, given the need for vegetation to place deeper roots in search of moisture or nutrients [1,5]. However, the emergence of crop marks depends on many factors, including the type of vegetation and soil, depth of burial, surface morphology and local environmental conditions [7–9]. In certain conditions, crop marks can even become more apparent following a period of rainfall [10].

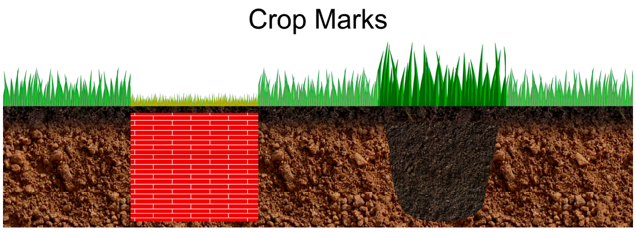

Figure 2. Crop marks: surface residues in the overlying vegetation of a buried wall (**left**) and a buried ditch (**right**).

Crop marks, soil marks and other archaeological residues may be detected on remotely sensed images whilst often they may not be visible on the ground [4]. From the beginning of the 20th century archaeological residues have been discovered in panchromatic air photos acquired from remote platforms, such as balloons and aircraft [3,11]. The high reflection of near-infrared (NIR) radiation by the cell structure of healthy green plants [12] can be exploited to better enhance differential vegetation health due to buried structures [9]. Combining various measurements in the range of Photosynthetically Active Radiation (PAR) (400 to 700 nm) that photosynthetic plants absorb [13], with measurements in the NIR, can be used to further enhance subtle differences in vegetation stress [14]. Much research has been carried out on the use of multispectral [8,15,16] and hyperspectral [17–19] data for the enhancement of crop marks, exploiting multiple image bands from the visible to the NIR parts of the electromagnetic (EM) spectrum. The thermal infrared (TIR) part of the EM spectrum has also been used to detect buried structures due to their heat signature [20], which can be enhanced through calculations of the day-night thermal inertia [21]. Studies have also shown that ultraviolet (UV) remote sensing can enhance the visibility of crop marks in certain conditions [22].

The unique nature of microwave remote sensing, with its cloud penetration capability and independence from solar illumination has also been used for archaeological prospection. It has mainly been employed in desert regions, exploiting the capability of active microwave systems to penetrate dry sand and directly detect buried structures [23–29]. Over vegetated soils in temperate regions the subsurface imaging capability of current Synthetic Aperture Radar (SAR) sensors is likely to be negligible [23]. However, SAR has other unique properties that may be exploited for the detection of surface residues of buried archaeological structures. The sensitivity of microwaves to the complex dielectric constant of materials translates to a sensitivity to the moisture content of soils [30]. Another consideration is that backscatter from SAR instruments depends on the roughness and geometry of targets. These properties may be suitable for the detection of soil or vegetation residues of buried archaeological structures. Moreover, interferometric SAR (InSAR) has long been capable of measuring subtle surface topographic variations [31]. A prerequisite for repeat pass InSAR topographic mapping is high coherence. In vegetated areas coherence is usually low, given the likelihood of temporal decorrelation due to random movement of individual scatterers at the scale of the SAR wavelength. However, with a large time series of data, such decorrelation effects can be minimized with techniques such as Small Baseline Subsets (SBAS), which generate interferograms that are selected to minimise the temporal baselines between acquisitions (and also the spatial baselines when used to measure displacement velocities) [32].

Some attempts have been made to detect surface residues of buried archaeological structures in vegetated regions using SAR data, most notably in Angkor Watt [33,34], in Costa Rica [35], in Italy [36,37], and in China [38], but these have limited their analysis to SAR backscatter intensity, often focussing on the use of polarimetric SAR (PolSAR). In some cases SAR derived Digital Elevation Models (DEMs) have been used to detect topographic anomalies in vegetated areas, but only those generated from single pass InSAR or from airborne platforms, most notably to detect "bajos" in Guatemala [39], to predict the location of archaeological sites in San Clemente Island, California [40], and in Angkor Watt, to detect elevated archaeological sites [34].

The aim of this study is to assess, for the first time, the use of both the amplitude and the phase of the SAR signal (in the form of filtered backscatter, coherence and interferometric time series) to detect surface residues of buried archaeological structures. A number of sites have been selected surrounding the area of Rome where archaeological survey data exists. Over these areas 77 COSMO SkyMed (CSK) Stripmap and 27 CSK Spotlight imagery have been procured. Processing included multitemporal filtering of backscatter, calculation of coherence between consecutive image acquisitions and SBAS DEM generation over each subset area. Surface residues of buried structures have been found in all three layers of backscatter, coherence and DEM. In an attempt to understand the mechanisms and conditions responsible for the appearance of residues in each layer, an analysis of results has been carried out with interferometric coherence and Potential Soil Moisture Deficit (PSMD) data (calculated from rainfall and potential evapotranspiration).

1.2. Study Areas

The Areas Of Interest (AOIs) chosen for this study comprise a number of small (most no more than 10 km^2) rural sites situated just outside the metropolitan area of Rome (see Figure 3). The land cover of each is mainly agricultural or pastural. The geology of the region is characterized by volcanic deposits (mainly pyroclastic tuff) from the Albano volcano district to the southeast and the Sabatino volcano district to the northwest, with alluvial sediments along the Tiber valley in between the two [41]. Figure 4 is a DEM of the area from the Shuttle Radar Topography Mission (SRTM). The topography gradually decreases from these two volcanic districts towards the Tiber, with valleys carved by fluvial erosion. The AOIs of Appia and Prenestina are located on the volcanic deposits of the Albano volcano, with undulating eroded valleys. The AOI of Veii is the site of an ancient Etruscan city perched on an area of volcanic deposits from the Sabatino district, in between valleys carved out from the tuff by fluvial erosion. The remainder of the AOIs are in the alluvial deposits of the Tiber, characterized by very flat topography: Salaria is in the Tiber valley, while Portus and Ostia are in the Tiber delta.

The climate of the AOIs is warm and temperate (Mediterranean), with cool winters and warm to hot summers. Figure 5 is a graph of rainfall and temperature in the time period of the SAR image acquisitions. In this period, the temperature almost every summer reached above 35 degrees centigrade, and in winters it seldom dropped below 5 degrees. The monthly rainfall was particularly high in November 2010 and November 2013, when it reached beyond 250 mm. In July and August of most years in the time period there was negligible rainfall [42].

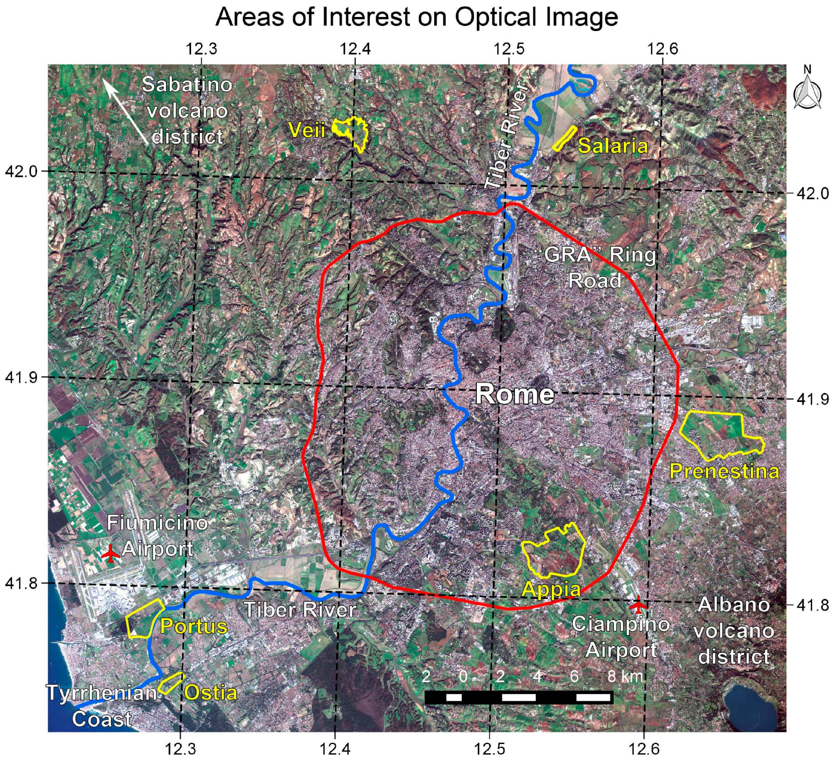

Figure 3. Areas Of Interest (AOIs) shown as yellow polygons on true colour, 10 m resolution Sentinel-2 image acquired on 28 December 2015 (bands 4, 3 and 2 displayed as red (R), green (G) and blue (B) respectively). Contains modified Copernicus Sentinel data 2016.

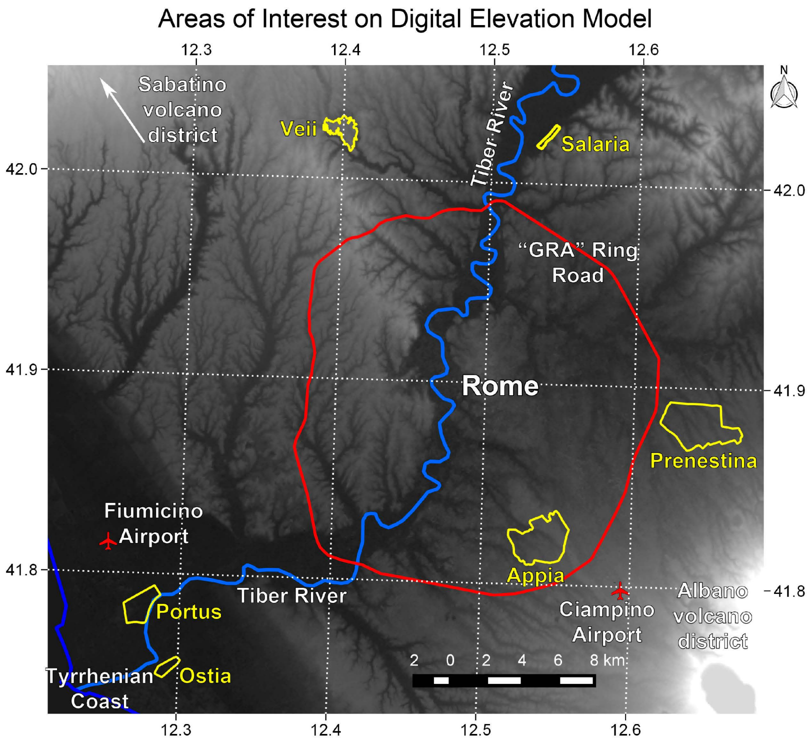

Figure 4. Shuttle Radar Topography Mission (SRTM) Digital Elevation Model (DEM) at a spatial resolution of 1 arc-second (30 m) with AOIs (yellow polygons) overlain. SRTM data courtesy of the United States Geological Survey (USGS, 2006).

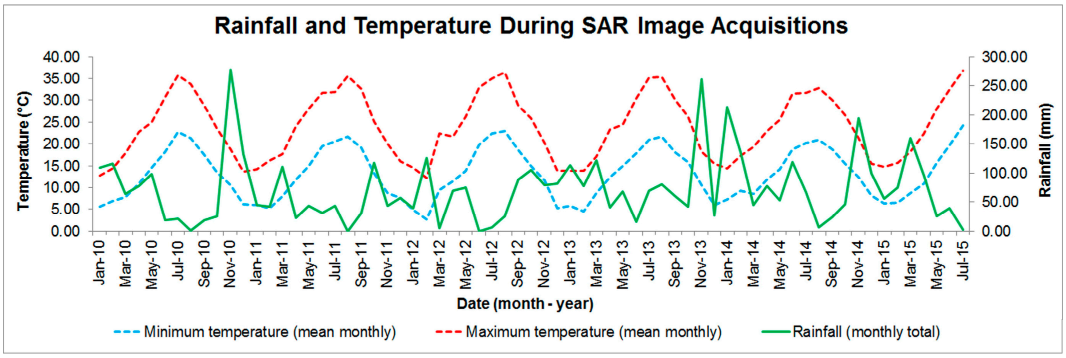

Figure 5. Graph showing rainfall and temperature in time period of Synthetic Aperture Radar (SAR) image acquisitions. The data from which the graph was produced was obtained from the Italian Hydrographic Office of the Lazio region (*Ufficio Idrografico e Mareografico*) [42].

All the AOIs are known to contain buried archaeological structures, mainly from the Roman to medieval periods. Some of these structures, perhaps not all, have been documented at various levels of detail following archaeological surveys including geophysical prospection, field walking or airborne or spaceborne optical remote sensing analysis [43–48]. A more detailed description of the archaeology, and other characteristics of each AOI, is described in the Results (Section 4).

2. Materials

SAR Data

Table 1 shows the characteristics of the COSMO-SkyMed (CSK) data. The CSK Stripmap images are all ascending pass, with a scene center incidence angle of 34 degrees and a polarization of Horizontal transmit and Horizontal receive (HH). 77 images were available in the e-geos catalogue with these characteristics over the AOIs at the time of the analyses. These were procured as they constituted the largest possible CSK Stripmap time series, with consistent geometry and polarization, that covered all AOIs.

Table 1. CSK data characteristics. For precise characteristics of all data, see Table S1 in the Supplementary Data section.

Number of Scenes	Sensor Mode	Acquisition Date Range	Polarisation	Pass	Scene Center Incidence Angle
27	ENHANCED Spotlight	June 2010 to August 2012	24 × HH 3 × VV	Asc	25.25
77	Stripmap HIMAGE	March 2011 to July 2015	HH	Asc	33.95

The 27 Spotlight images also comprised the largest possible time series of CSK Spotlight data over any of the AOIs. For the CSK Spotlight coherence analysis, only the HH images were used since InSAR is very sensitive to differences in polarisation and a consistent dataset was required. For the CSK intensity time series analysis on the other hand, both the HH and Vertical transmit and Vertical receive (VV) images were used, since this analysis is less sensitive to changes in polarisation. For more precise characteristics of all data, including individual scene record numbers, see Table S1 in the Supplementary Data section.

3. Methods

Three types of SAR information layers were created from which surface residues of buried archaeological structures were detected and analysed: multitemporal speckle filtered σ^0 backscatter, interferometric coherence and SBAS DEM. The methodologies of each are described respectively in Sections 3.1–3.3. Extracted features were analysed with meteorological data and interferometric coherence in an attempt to determine the cause of the appearance of features in the various SAR layers, the methodology of this is described in Sections 3.4 and 3.5.

3.1. Multitemporal Speckle Filtered σ^0 Backscatter

All 77 CSK Stripmap images in Single Look Complex (SLC) format were subsetted for each AOI and the 27 Spotlight SLC images were subsetted for the Prenestina AOI. The stacks over each AOI were then coregistered with the aid of the SRTM 1 arc-second (30 m) DEM. Over Prenestina each CSK image mode was coregistered separately. The images were then multilooked by a factor of 1×1 (CSK pixel dimensions are square at SLC), only to remove the phase component and convert the images from SLC to detected.

Multitemporal De Grandi speckle filtering was then applied to each stack. Conceptually, the De Grandi filter works by averaging in the temporal domain parts of images that are statistically homogenous. If such an area is interrupted by the appearance of a feature in one or more images, the areas to be averaged are divided to exclude this feature [49]. The De Grandi filter preserves the spatial resolution of the input images. Small scale structures in individual images are retained, making it suitable for identifying small anomaly features with only slight variations in backscatter from surrounding areas [49,50].

The speckle filtered imagery was then geocoded to the Universal Transverse Mercator (UTM) projection (Zone 33 North), with the World Geodetic System 1984 (WGS 84) datum. Terrain correction was performed with the SRTM 1 arc-second DEM. The pixel spacing of the CSK Stripmap imagery was set to 2.5 m and the CSK Spotlight to 1 m.

The imagery was calibrated to σ^0 and converted to decibel (dB).

3.2. Interferometric Coherence

The interferometric coherence is a measure of the small scale randomness of the phase difference between coherent SAR signals. High coherence corresponds to no random difference, while low coherence corresponds to a high degree of randomness [51]. Loss in coherence may be due to many factors, one of which is the extent of small scale random movement, between image acquisitions, of individual scattering elements, such as leaves in vegetation blown by wind. This is referred to as temporal decorrelation [52].

The interferometric coherence was calculated between consecutive image acquisitions covering each AOI that have a temporal baseline of 16 days. In the case of the CSK Spotlight data, coherence was calculated between images with temporal baselines of 16 days and 1 day.

Prior to coherence generation, each SLC image pair was coregistered with the aid of a DEM (SRTM 1 arc-second). The coherence was then calculated over a window size of 5×5 pixels. Given the low resolution of the DEM compared to the CSK data, the local topographic phase was estimated in a 7×7 window and removed before coherence calculation.

The coherence images were then geocoded in the same way as that described in Section 3.1.

Coherences were plotted against the acquisition dates of both the master and slaves in all coherence charts displayed in the results (Section 4).

3.3. DEM

Given that SAR is a coherent system, the phase difference between SAR image acquisitions, separated by a perpendicular baseline, can be used for accurate terrain measurements [51]. Over vegetated areas, often temporal decorrelation prohibits the use of repeat pass InSAR for DEM generation [52]. However, with a large time series of data, this limitation can be overcome with techniques such as Small Baseline Subsets (SBAS). As described in Section 1.1, the SBAS technique generates interferograms that are selected to minimise the spatial (for displacement velocities) and temporal baselines between acquisitions, thus avoiding decorrelation effects [53]. While SBAS is primarily a technique for displacement measurement, it can also be used for DEM generation.

Over each study area, an attempt was made to generate a DEM using the SBAS technique with the available data. Given the high proportion of vegetation in all AOIs, the technique only worked well over the Prenestina AOI. However, over the Salaria AOI, despite the low coherence affecting most interferograms and/or the excessively small or large baselines, one interferogram (albeit noisy) clearly revealed the ancient Via Salaria. A DEM was therefore created from this pair alone using standard InSAR, without the need for SBAS processing.

The interferometric work flow was carried out using the ENVI SARscape software (version 5.2), the processing chain is shown in Figure 6. This is described in more detail for the Prenestina AOI in Section 3.3.1, and for the Salaria AOI in Section 3.3.2.

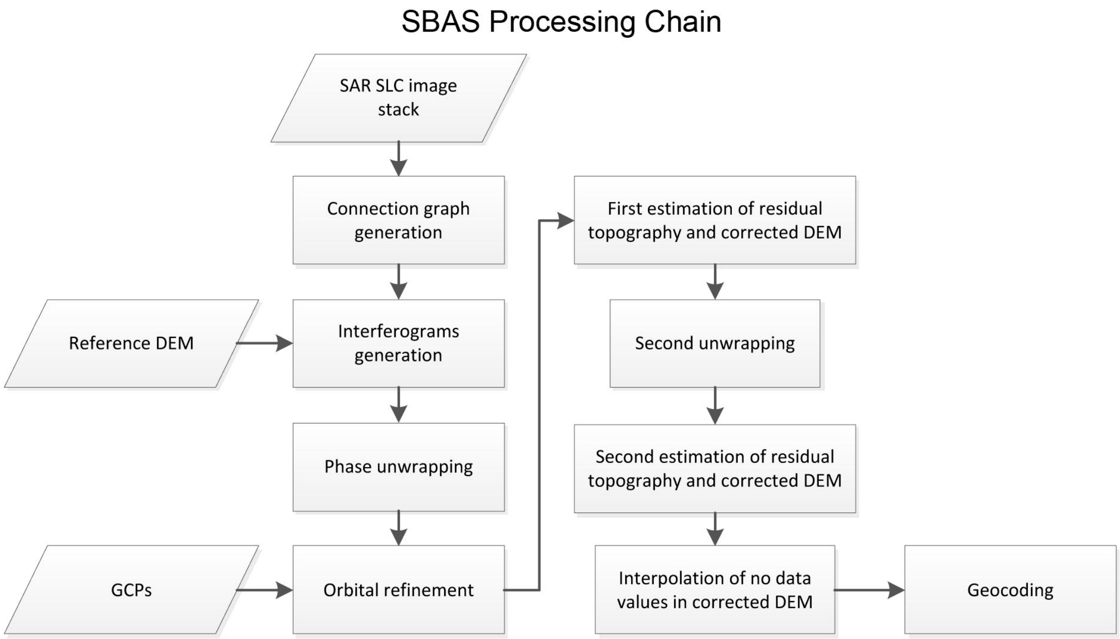

Figure 6. Flow chart showing the Small Baseline Subsets (SBAS) processing chain. This was implemented for both the CSK Stripmap and Spotlight time series using the SARscape software (version 5.2).

3.3.1. SBAS DEM: Prenestina AOI

With the availability of a time series of both Stripmap and Spotlight CSK data over the Prenestina AOI, two SBAS DEMs were created: the first using the Stripmap data, with the SRTM 1 arc-second DEM as a reference; the second using the Spotlight data, with the Stripmap SBAS DEM as a reference. The SBAS processing of the Stripmap data was therefore simply an intermediate step in the creation of the final SBAS DEM derived from the Spotlight data.

The first step in the SBAS process is to determine which image pairs to utilise to create interferograms [32]. This can be displayed graphically as a two dimensional plot (connection graph) showing the temporal and spatial baselines of the interferometric pairs. Figure 7 shows the connection graph of the Spotlight acquisitions. For both the Stripmap and Spotlight SBAS processing, image pairs were connected only if their perpendicular baselines were from 0 to 35 percent of the critical baseline, and if their temporal baselines were from 0 to 17 days. Disconnected blocks were permitted given that calculation of displacement velocities was not required.

Interferometric processing was then carried out for each connected image pair. This included DEM assisted coregistration, interferogram generation, interferogram filtering (Goldstein), coherence calculation and phase unwrapping (Minumum Cost Flow). A reference DEM was required for the DEM assisted coregistration and for topographic fringe removal to assist with the phase unwrapping.

For the Stripmap data the SRTM (1 arc-second) DEM was used, while for the Spotlight data the Stripmap SBAS DEM was used.

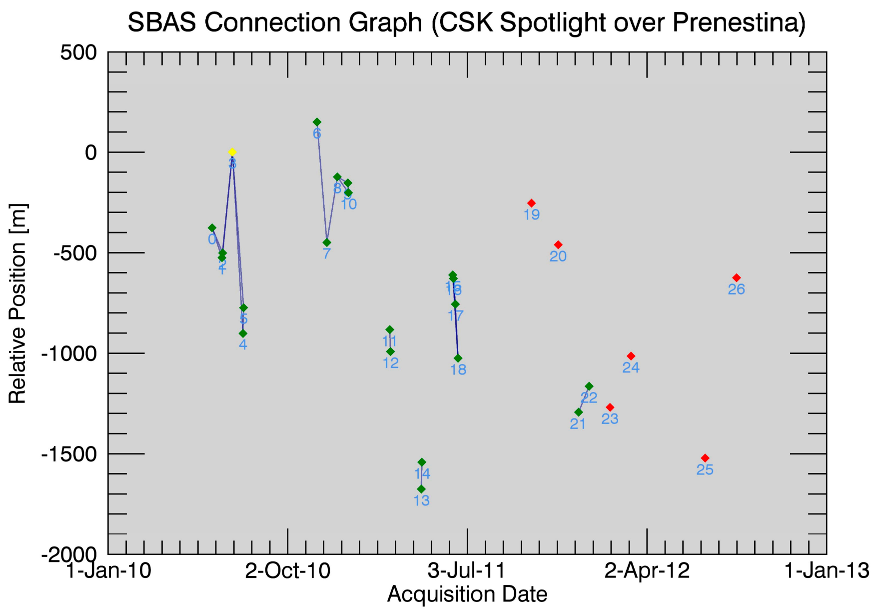

Figure 7. SBAS connection graph for the CSK Spotlight data. Connected pairs are shown that have perpendicular baselines from 0 to 35 percent of the critical baseline, and temporal baselines from 0 to 17 days. Disconnected blocks are permitted given that displacement velocities are not required to be calculated. Selected and discarded images are displayed respectively as green and red points. The yellow point shows the super master image.

The unwrapped interferograms were inspected. Connections yielding very noisy results were removed. In some cases, the unwrapping was repeated with the unwrapping coherence threshold readjusted.

On the selected remaining unwrapped phase images, Ground Control Points (GCPs) were placed over stable areas (mainly roads) and the unwrapped phases re-flattened to remove phase ramps due to orbit inaccuracies.

A first inversion was applied to the re-flattened, unwrapped interferograms to obtain the residual topography. Following this, a second unwrapping was performed as a further refinement. These final unwrapped interferograms were then used as input to a second inversion. The final DEM in slant range was produced following the second inversion.

The slant range DEM was geocoded to UTM zone 33 N, WGS 84. Some gaps in the DEM where the coherence was below the threshold for the phase unwrapping were interpolated.

3.3.2. InSAR DEM: Salaria AOI

During the SBAS process for the Salaria AOI, for all the interferometric pairs but one, either the coherence was very low, or the baselines were too large or small to permit DEM generation. However, during the inspection of the flattened interferograms, the trace of the ancient Via Salaria was very clearly visible in one flattened interferogram produced from the image pair acquired on the 10 and 26 August 2012. Even this interferogram had low coherence throughout most of the image, but less so than most of the other interferograms. The perpendicular baseline was 307 m and the altitude of ambiguity 21.6 m. It was decided therefore to produce a DEM over the Salaria AOI with only this image pair as a standard InSAR procedure, rather than using SBAS with the entire time series.

Due to the low coherence, the final DEM was very noisy, and no accurate absolute or relative heights could be derived from it. However, as a purely qualitative result, it was nonetheless possible to trace the line of the ancient Via Salaria in the DEM. This is discussed further in the results, Section 4.

3.4. GIS

All SAR products were imported into a Geographic Information System (GIS) [54] (using the software QGIS version 2.8.1) and compared with archaeological charts, optical images and DEMs.

Both the interpretation of the magnetometry survey published by Keay et al., 2005 [43] over the Portus AOI, and the map showing documented archaeological features by Quilici, 1974 [46] in the Prenestina AOI, were manually geometrically corrected by the author by collecting GCPs using the geocoded Pleiades imagery as a reference, and resampling the images using a first order polynomial. These could subsequently be superimposed on the SAR images in the GIS for comparison.

3.5. Analysis of Features

Having identified surface residues in the SAR data over locations in which buried archaeological structures are known, or suspected, to exist, the next step involved an in-depth analysis of these to attempt to understand why, and under what conditions, these residues are visible (or not visible) in the various SAR derived products of filtered σ^0 backscatter, coherence and DEM. To achieve this, first the clarity (contrast) of identified features was quantified. This enabled the quality of archaeological residues to be compared in SAR products over time, and to be correlated with possible contributing factors relating to meteorological, vegetation and soil conditions.

3.5.1. Mean Ratio Detector (MRD)

To quantify the clarity of the identified archaeological residues, the standard Mean Ratio Detector (MRD) method was applied, as described in [55]. The MRD calculates the ratio of the local means of two areas as a measure of their difference in backscatter intensity according to the following expression:

$$r_{\mathrm{MRD}} = 1 - \min\left\{\frac{\mu X}{\mu Y}, \frac{\mu Y}{\mu X}\right\} \tag{1}$$

where μX and μY are the mean values of two subset regions [55]. The subset regions in this case comprise a region over the archaeological residue and a region outside but nearby (in some cases an average of two regions on either side of the archaeological residue). In the case of the σ^0 backscatter images, the subset regions were extracted from the un-filtered images in linear scale.

3.5.2. Potential Soil Moisture Deficit (PSMD)

SAR is sensitive to variations of relative permittivity, which in soils is mainly determined by the presence of moisture. The higher the quantity of moisture in the soil, the higher the relative permittivity, which in turn produces a higher SAR backscatter [23,30,56]. SAR is also sensitive to roughness relative to the SAR wavelength [23], which may be affected by differential crop growth. As described in Section 1.1, a key contributing factor in the formation of many archaeological crop marks is moisture, in particular a moisture deficit which may exacerbate differential crop growth [1,3,5,10,15]. It is hypothesised therefore that there may be a correlation between archaeological residues in the SAR data and soil moisture. To test this hypothesis, the "Potential Soil Moisture Deficit" (PSMD), as described by Jones and Evans, 1975 [1], was calculated over each AOI and for each day from a month prior to the first CSK image acquisition to the date of the last CSK acquisition. The PSMD is a measure of the water available to plants. It is calculated as a difference between potential evapotranspiration and rainfall and is an approximation of actual Soil Moisture Deficit (SMD), which requires knowledge of soil and plant parameters. PSMD, on the other hand, is purely a meteorological concept [1]. Here it is calculated as the difference between local potential evapotranspiration using the Penman-Monteith formula [57], and local rainfall for each AOI individually.

Soil moisture datasets are available, such as those derived from the Advanced Scaterometer (ASCAT) of the Metop satellite [58], and from the Soil Moisture and Ocean Salinity (SMOS) satellite mission [59], but the spatial resolution of the data (25 km for ASCAT and 50 km for SMOS) was deemed too coarse for such high resolution analysis. It may have been possible to derive soil moisture directly from the CSK SAR data, but accurate SAR derived soil moisture retrieval is particularly challenging given the difficulty in separating backscatter variations due to dielectric differences from those due to roughness, with the latter usually exerting a greater influence [56]. It was decided therefore to derive information on soil moisture from calculations of PSMD using data from the extensive local network of weather stations maintained by the Italian Hydrographic Office of the Lazio region (*Ufficio Idrografico e Mareografico*) and the Italian Agricultural Innovation and Development Agency for the Lazio region, ARSIAL (*Agenzia Regionale per lo Sviluppo e l'Innovazione dell'Agricoltura del Lazio*).

Calculation of PSMD requires measurements of potential evapotranspiration and rainfall. The potential evapotranspiration data, in mm per day, was obtained on request from ARSIAL. Data was obtained from several stations, including: Fiumicino, Maccarese (UTM 33N (*X*): 271.379, (*Y*): 4.633.596); Roma, Via Lanciani 38 (UTM 33N (*X*): 294.721, (*Y*): 4.644.111); and Roma, Ponte di Nona (UTM 33N (*X*): 305.016, (*Y*): 4.641.204). For each AOI, data from the station nearest the AOI was selected, and where there were gaps, these were filled by data from the next nearest station.

The rainfall data was obtained from the Italian Hydrographic Office of the Lazio region. Daily rainfall data is available from a dense network of stations through their website [42]. The data, in mm per day, was procured from the following weather stations: Isola Sacra, Ostia, Maccarese, Tor Vergata, Salone, Capannacce, Castelgiubileo, Fidene, Roma Nord and Monterotondo. The locations of these are shown on the Lazio Hydrographic Office website [42]. As with the evapotranspiration data, for each AOI, the rainfall data from the weather station nearest to the AOI was obtained, and where there were gaps, these were filled by data from the next nearest station.

To calculate the PSMD, first the daily potential evapotranspiration was subtracted from daily rainfall, then the sum of this difference for the last 30 days was calculated. This was done for each day in the time period of CSK image acquisitions. Negative values correspond to PSMD while positive values correspond to a Potential Soil Moisture Surplus (PSMS).

Finally, the PSMD was correlated with the clarity of archaeological residues in the various SAR products, and over time (see Section 4).

3.5.3. Coherence

Another key factor in the formation of archaeological residues in the SAR data products includes the state of vegetation. It may be that the archaeological residues in the SAR data are soil marks in fallow fields, or crop marks. Lacking precise information on the type of vegetation in each field of each AOI, an attempt was made to extract some information on the state of vegetation from the interferometric coherence. The temporal baseline between most of the consecutive CSK Stripmap acquisitions was 16 days, while for the Spotlight data, the most common temporal baselines were 16 days and 1 day.

Studies have shown inverse relationships between vegetation height and coherence at various SAR frequencies, including at X-band and with COSMO SkyMed [60,61]. However, with X-band, complete temporal decorrelation is soon reached with vegetation growth and short temporal baselines are necessary to derive quantitative information on crop height [60,61]. Moreover, the rate of temporal decorrelation depends on many factors, such as crop type, moisture and wind [62]. Another factor to take into account is the perpendicular baseline [51], which in the case of COSMO SkyMed, can vary considerably between image acquisitions. Given the complexity in establishing a quantitative relationship between coherence and crop height that takes into account these variables, and given primarily the long temporal baselines (16 days for the Stripmap data), the coherence calculated here provided only a rough qualitative idea of the ground conditions. For example, if very high coherence is observed in a particular field, this may be interpreted in different ways through analysis of the time series: it may coincide with a period in which the field is fallow, or if the high coherence is observed over a longer time period, the field may be occupied by a crop or structure characterized by little random movement (such as beanstalks tied to poles). To obtain consistent datasets, for the Stripmap data only the coherence between InSAR pairs with 16 day baselines were considered, while for the Spotlight data, both 1 and 16 day baseline pairs were considered as separate datasets.

4. Results

Comparison of the SAR data with the archaeological charts over all AOIs revealed archaeological residues in Portus, Prenestina and Salaria. No archaeological residues were identified in Appia or Veii. Over Ostia only very faint traces were observed which were difficult to quantify. An in-depth analysis of the AOIs, and the residues identified in them, is provided in this section. Each AOI is shown on a NIR, red (R) and green (G) colour composite of an optical satellite image, to highlight the vegetation characteristics. In Prenestina, the same residues were observed in both the CSK Spotlight and Stripmap data. Given that the clarity of these in all the SAR product types of filtered σ^0 backscatter, coherence and DEM was enhanced in the Spotlight data, the analyses for Prenestina is limited to the Spotlight data.

4.1. Portus

The AOI of Portus is located between the hexagonal harbour of Trajan to the west, the Tiber river to the east, the "Fossa Traiana" to the south and the A91 Rome to Fiumicino highway and railway line to the north (Figure 8). Being in the Tiber delta, the area is very flat with an alluvial substrate [63]. Today the AOI is in a region comprising irrigated fields of arable crops [43,64]. It is traversed by a number of roads and there are some isolated farm buildings. To the west the area is more built-up and there are a greater number of trees.

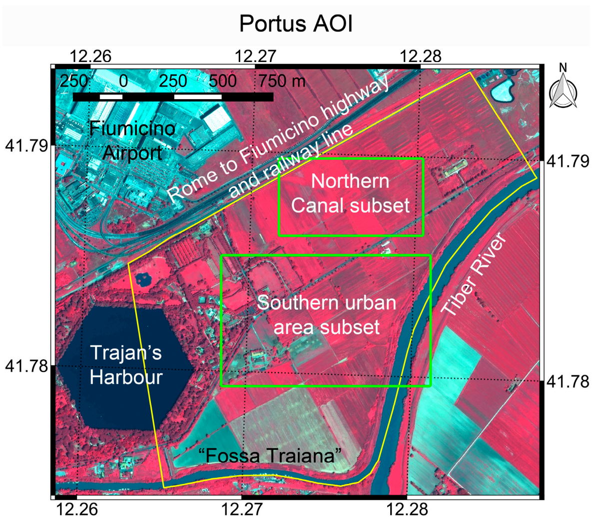

Figure 8. Portus AOI shown as yellow polygon on Pleiades image acquired on 8 May 2014. The Northern Canal and southern urban area subsets are shown by the green rectangles. The image was pan-sharpened to 0.5 m spatial resolution, and is displayed as NIR, R and G respectively as R, G and B. Pleiades data provided by the European Space Agency.

The archaeology of the area is dominated by the presence of the ancient port of Rome, in particular, the hexagonal harbour of Trajan. Construction of Trajan's harbour began in 100 AD as an enlargement of the artificial harbour initiated by Claudius in 42 AD and continued by Nero. The harbour complex, known as Portus, replaced Ostia as the principal port for the city of Rome up to the Byzantine period. While the coastline remained stable throughout the Roman period, it has since migrated seawards by several kilometres due to a combination of neotectonic movements, sea-level changes and sediment load variations of the Tiber River. The harbour of Portus would have silted up in post-Roman times [43,65].

Much archaeological research in this area has been carried out over the years, particularly by Lanciani [66], Lugli and Filibeck [67], Testaguzza [68], and more recently, by the Portus Project. The Portus Project involves extensive non-destructive archaeological survey of Portus including geophysical prospection (particularly magnetometry), air photo interpretation and systematic surface collection. The project began in 1997 and is on-going. The work is undertaken by the Soprintendenza per i Beni Archeologici di Ostia, the British School at Rome, and the Universities of Southampton, Durham and Cambridge [43,65]. It is primarily the results of this project (which integrates also the results of previous research) that has been used to compare with the results of the SAR data analysis.

Many archaeological structures are situated near the hexagonal harbour of Trajan (see Figure 8). In the open fields between the lake and the Tiber, the most significant buried structures identified to date include a canal to the north, referred to as the Northern Canal, and a canal to the south, along which ran a gravel road, aqueduct and various buildings. Near to the Tiber, the aqueduct changed direction to enclose a trapezoidal area between it and the Tiber. The region between the aqueduct and the Tiber appears to have been densely developed [43].

Many of the larger buried archaeological structures mapped by the survey are also visible as residues in the filtered σ^0 backscatter images. These include the Northern Canal and the built-up area in between the road and canal to the south, and in between the aqueduct and the Tiber river. No residues are present on the coherence images. The Northern Canal and built-up area to the south are treated as two subset areas, as shown in Figure 8. It is difficult to derive any information on buried structures from the SAR data near the hexagonal harbour of Trajan due to the high density of trees and buildings in this area.

4.1.1. Portus Northern Canal

The Northern Canal is recorded in an inscription as having been constructed under the Emperor Claudius for flood relief. It was cut into the natural alluvium and had earth embankments. It connected the Tiber river to the sea. The width of the canal, as measured in the survey of Keay et al. 2005, seems to vary between 20 and 35 m [43].

Figure 9a shows a residue of the Northern Canal on an image of filtered σ^0 backscatter acquired on 16 November 2011. This is one of the clearest images of this residue on the σ^0 images. Figure 9b shows the same image with the interpretation of the magnetometer survey in [43] superimposed. Figure 10 is an optical Pleiades satellite image, covering the same extent as in Figure 9. It has been pan sharpened to 0.5 m spatial resolution, and displayed as a NIR, R and G colour composite. The yellow arrow points to the location and direction from which the photograph in Figure 11 was acquired. All residues of this feature appear in higher backscatter than surrounding areas. No traces of the feature are evident on the ground, as observed on 24 May 2013 (see photo acquired on that date in Figure 11). Traces are sometimes visible on optical air photos and satellite imagery. These are enhanced in the NIR (as in Figure 10).

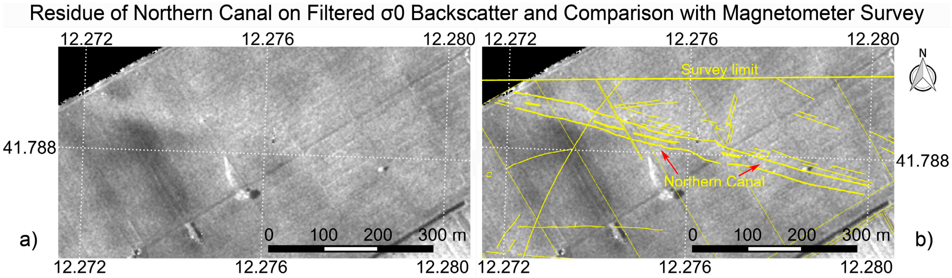

Figure 9. (**a**) Residue of Northern Canal on image of filtered σ^0 backscatter acquired on 16 November 2011; (**b**) Overlain with features interpreted by magnetometry survey published by Keay et al., 2005 [43]. COSMO SkyMed data provided by the Italian Space Agency. Vectors of interpreted features, copyright Keay et al., 2005 [43].

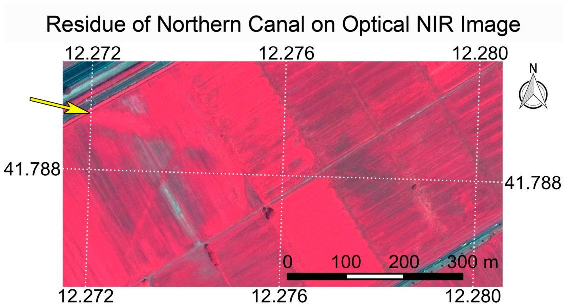

Figure 10. Residue of Northern Canal on Pleiades image acquired on 8 May 2014, pan-sharpened to 0.5 m spatial resolution. NIR, R and G displayed as R, G and B respectively. Yellow arrow shows direction and location from which photo in Figure 11 was acquired. Pleiades data provided by the European Space Agency.

Figure 11. Photo acquired over site of Northern Canal on 24 May 2013 at 18:45 Central European Time (CET). No traces are evident of the Northern Canal. The shadow of the photographer in the center shows the direction of the sun. The location and direction from which the photo was acquired is shown in Figure 10.

4.1.2. Portus Southern Urban Area

This area is also crossed by a canal, which was constructed under Trajan. It was approximately 35 m wide and the magnetic survey of Keay et al., 2005 reveals that it was probably flanked by wide walls, about 3 or 4 m wide, that may have acted as towpaths. The canal connected the Fossa Traiana with the Tiber (see Figure 8) and was probably used for navigation. To the north of the canal was a road, about 15 m wide. However, the magnetic survey only noted the kerbs of this road. It is likely therefore that it had only a gravel surface rather than stone paving. To the north of the road passed an aqueduct, which was carried on piers. The geophysical survey revealed two phases of development of the aqueduct: the first phase predated the canal and road, while the second took place in the Trajanic period, probably at the same time as the canal and road were built. In between the canal and the road, a series of buildings have been detected by the geophysical survey. Also, as the aqueduct changes direction and forms a trapezoidal area between it and the Tiber, the area in between the Tiber and the aqueduct seems to have been densely developed. Surface ceramics from these areas suggest construction began primarily from the second century onwards. Development was thought to have been stimulated by the presence of the canal and road [43].

Figure 12a is a subset of a filtered σ^0 backscatter image acquired on 9 July 2012. This is one of the images that best reveals residues of the buried urban structures in this area. These buried urban structures are between the canal (to the south) and the gravel road and aqueduct (to the north), and between the aqueduct, further to the north, and the Tiber river. Other structures, such as the canal, road and aqueduct, do not appear as residues in any of the SAR images. In all images in which traces of these urban structures are visible, they are visible as areas of lower backscatter relative to surrounding areas. Figure 12b shows the interpretation of the archaeological survey of Keay et al. [43] overlain. The vast majority of the features identified in this survey were from magnetometry prospection, but a few structures were identified in crop marks on air photos, such as the isolated building to the west of the aqueduct as it travels roughly parallel to the Tiber. Figure 13 is another subset of the same Pleiades image as in Figure 10, also pan-sharpened and displayed in the same band combination. Some of these structures are also faintly visible in this Pleiades image.

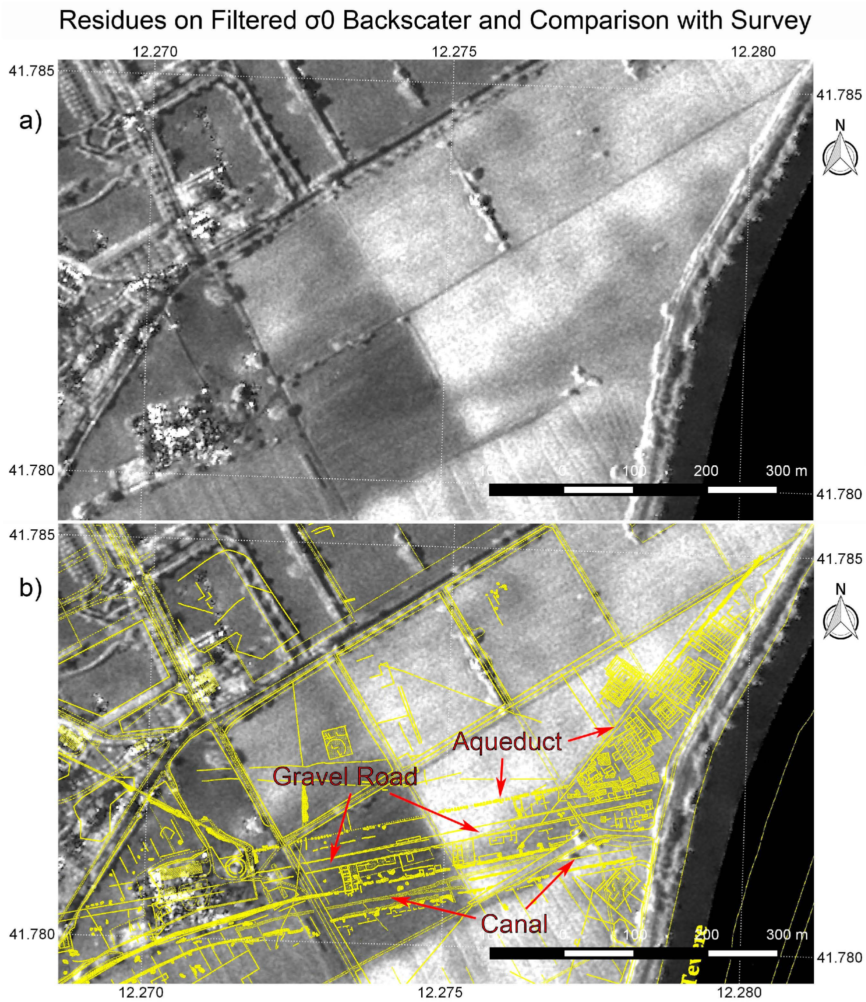

Figure 12. (**a**) Residue of buried buildings on image of filtered σ^0 backscatter acquired on 9 July 2012; (**b**) Interpretation by Keay et al., 2005 of integrated archaeological survey (mainly magnetometry) published in [43] overlain. The residues in the SAR image correspond to the built-up areas, not to the canal or the gravel road. COSMO SkyMed data provided by the Italian Space Agency. Vectors of interpreted features, copyright Keay et al., 2005 [43].

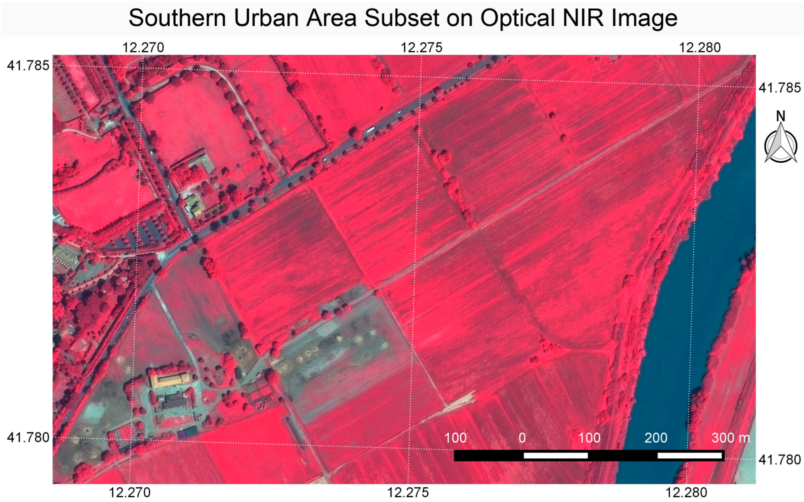

Figure 13. Southern urban area subset of Portus AOI (same extent as Figure 12) on Pleiades image acquired on 8 May 2014, pan-sharpened to 0.5 m spatial resolution. NIR, R and G displayed as R, G and B respectively. Pleiades data provided by the European Space Agency.

4.1.3. Portus Features Analysis

Figure 14 shows the location of subset areas extracted over and outside of each of the residue areas in the Portus AOI for the MRD contrast analysis. Figure 15 shows the contrast of the residues in the σ^0 backscatter over time, and plotted with PSMD. No clear correlation in the clarity of the two features over time is present. Perhaps this is not surprising, given that the two residues are of a completely different nature (possibly manifestations of positive and negative crop marks respectively). The contrast of neither residue appears to correlate with PSMD. However, this may not play a role if the residues are situated in irrigated fields [64].

Figure 16 shows the contrast of residues in the σ^0 backscatter with residue coherence over time, while Figure 17 compares them in a scatter plot. Over the Northern Canal residue, in most cases, high contrast in the σ^0 backscatter is observed with high coherence. The image pair acquired between 22 April and 8 May 2011, for example, has a coherence of 0.68 over a temporal baseline of 16 days. In both images the Northern Canal residue appears clearly (see Figure 18). The coherence prior to this date is unknown, as there is a gap in the interferometric time series of six months. However, in the following interferometric pair (from 8 to 24 May 2011), the coherence drops to 0.31 (approximately the same coherence value as in the surrounding fields), and the canal contrast also drops in the σ^0 backscatter. As mentioned in Section 3.5.3, very high coherence may be observed over a fallow field, or over a field of crops characterized by very little movement, such as dried stems or crops tied to poles. In both cases, it is possible that the cause of the residue is in the soil. It may be therefore that the residues of the Northern Canal in the images acquired on 22 April and 8 May 2011 are soil marks. Between the image pair acquired on 13 and 29 October 2012 there is also a high coherence of 0.52 over the Northern Canal residue. Also in this case the residue is clearly present in the σ^0 backscatter of both images. Before and after this image pair, the contrast of the residue rapidly declines, as does the coherence. Where there is low coherence and high residue clarity, the residue may still be a soil mark, only there may have been some change to the field, such as rainfall, strong winds or human activity sufficient to reduce the coherence.

Over the southern feature, the residues appear with greatest clarity at times of low coherence. The fact that the residues appear as areas of lower than surrounding backscatter (in contrast to the Northern Canal) may be a result of negative crop marks. This could be explained by the buried urban structures hindering vegetation growth, as described in Section 1.1.

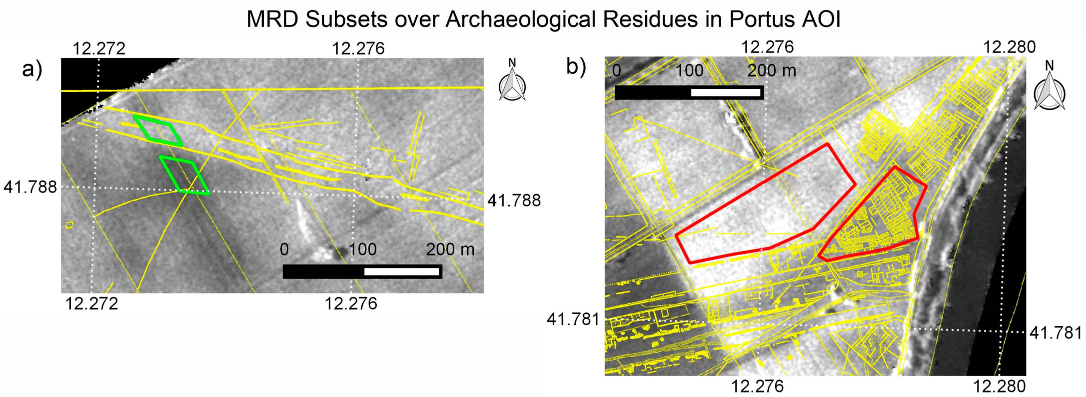

Figure 14. Subset areas used for Mean Ratio Detector (MRD) contrast analysis shown as: (**a**) green polygons, over and outside of a part of the Northern Canal residue; and (**b**) red polygons, over and outside of a part of the southern urban area residues. Polygons are overlain on the image of filtered σ^0 backscatter acquired on 16 November 2011. COSMO SkyMed data provided by the Italian Space Agency.

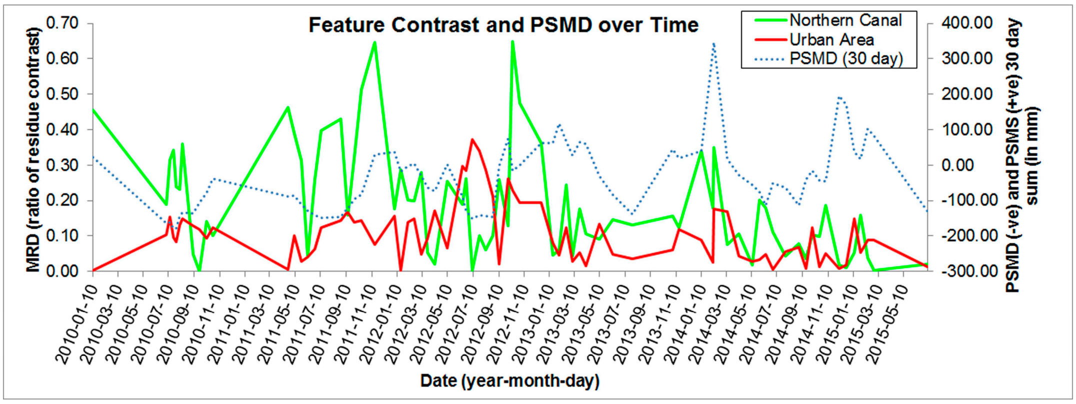

Figure 15. Graph showing clarity (contrast) of the two archaeological residues of the Northern Canal (in green) and the southern urban area (in red), plotted over time and with PSMD. The clarity of residues is quantified as a ratio (MRD). For the PSMD, negative values correspond to high PSMD (dry conditions), while positive values correspond to high PSMS (wet conditions).

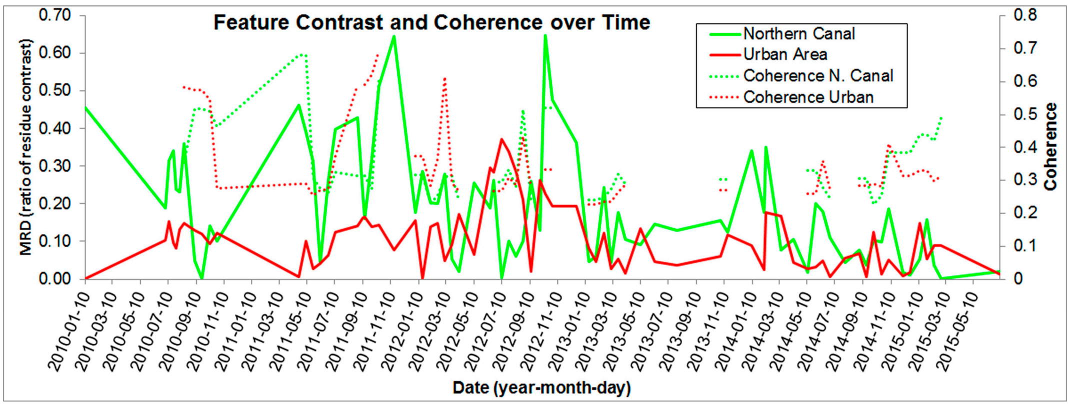

Figure 16. Graph showing contrast, quantified by means of MRD, of the two archaeological residues of the Northern Canal (in green) and the southern urban area (in red), plotted with their respective coherences (dotted lines) over time. The coherence values are provided both for the master and the slaves of InSAR pairs. Where a master is also a slave, it takes the value of the slave.

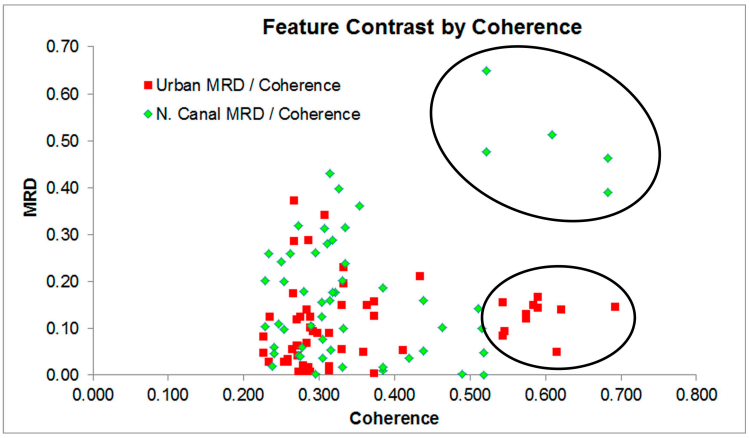

Figure 17. Graph showing contrast, quantified by means of MRD, of the two archaeological residues of the Northern Canal (in green) and the southern urban area (in red), plotted against their respective coherences. Where high coherence is observed, the contrast of the Northern Canal residue is often high, while the contrast of the southern urban area is consistently low. These patterns are shown in black ellipses.

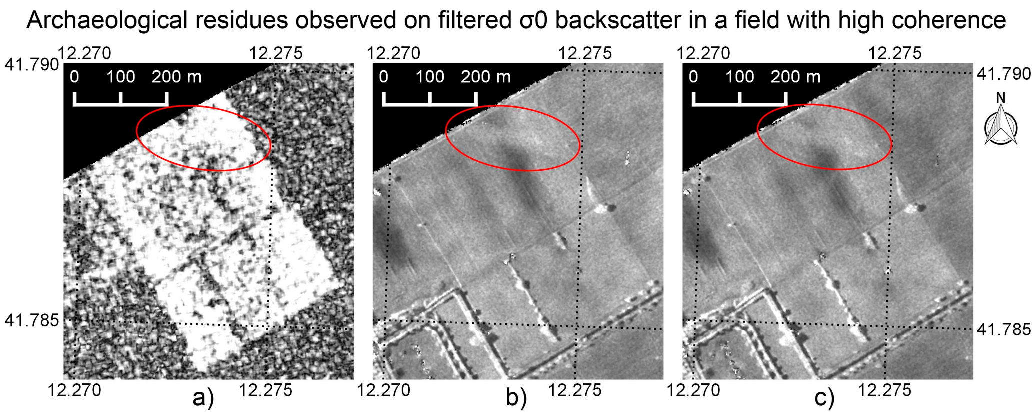

Figure 18. Example of a case in which very high coherence is observed over some fields in the CSK Stripmap pair with a temporal baseline of 16 days: from 22 April to 8 May 2011 (**a**); Residues of the buried Northern Canal are visible in the filtered σ^0 backscatter of both images of the pair, shown as red ellipse on filtered σ^0 image acquired on 22 April (**b**) and 8 May (**c**). COSMO SkyMed data provided by the Italian Space Agency.

4.2. Ostia

The AOI of Ostia is bordered to the north and west by the excavated part of the ancient Roman port city of Ostia, to the east by the Viale dei Romagnoli, and to the south west by the Via di Tor Boacciana (which also traverses the centre of the AOI) (see Figure 19). It is situated very close to the Portus AOI, and is also in the Tiber delta, thereby characterised by very flat topography and alluvial substrate [63]. The area today comprises fields of grass, dotted with the occasional tree. The soil is of class 3, with notable limitations mainly due to stoniness and shallow depth (as a result of the buried structures), and possibly also to poor texture or chemistry [69].

The ancient city of Ostia predates Portus. Historical accounts state the city was founded, as a colony of Rome, in the seventh century BC. However, the oldest archaeological remains date back only to the fourth century BC [70]. Following the construction of Portus, Ostia gradually fell into decline and was eventually abandoned in the 9th century AD [71].

Extensive excavations were carried out in Ostia from 1938 to 1942 for the World Exhibition of 1942 in Rome. However, around 50 to 60 per cent of the area remains unexcavated [44]. In the fields of the AOI, buried streets and buildings continuing from the excavated part of Ostia have been identified as crop marks in air photos and in geophysical surveys carried out by Becker and his team [44]. An attempt was made by Linck et al. to identify archaeological residues over the same area surveyed by Becker and his team using TerraSAR-X High-resolution Spotlight (1 m resolution) data acquired in October 2012 in the experimental 300 MHz bandwidth. Only a few faint traces of buried structures were visible [72]. Also in the analysis of the CSK filtered σ^0 backscatter described in this paper, only a very few faint traces were observed, which were difficult to quantify or unequivocally attribute to buried archaeological structures. No structures were identified in the coherence time series, which was characterized throughout by low coherence. This also inhibited InSAR or SBAS DEM generation.

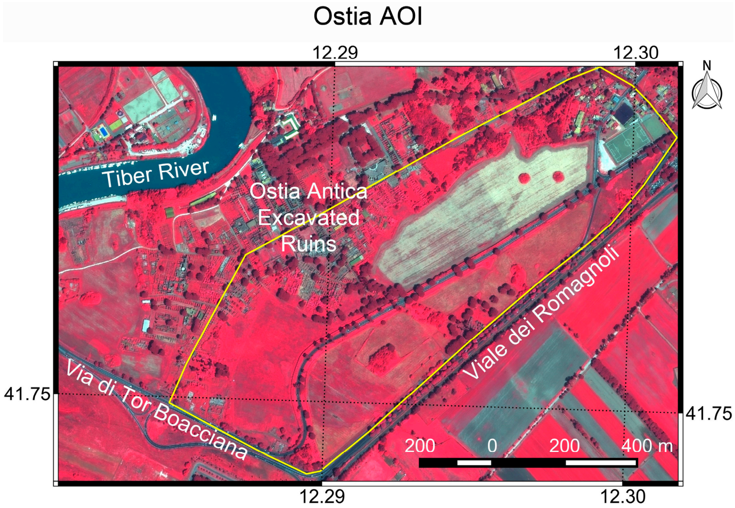

Figure 19. Ostia AOI shown as yellow polygon on Pleiades image acquired on 8 May 2014. The image was pan-sharpened to 0.5 m spatial resolution, and is displayed as NIR, R and G respectively as R, G and B. Pleiades data provided by the European Space Agency.

4.3. Appia

The AOI of Appia comprises the area selected by the project “Mapping the Via Appia”. This area surrounds a part of the ancient Appian Way at the 5th Roman mile from its origin in Rome. It is bordered to the north by the Via di Tor Carbone, to the south by the Via Torricola, to the east by the Via Appia Nuova and to the west by the Via Ardeatina. The AOI is within the “Parco Regionale dell’Appia Antica”. This is one of the larger AOIs. Figure 20 shows the location of the AOI on a NIR colour composite image. Figure 21 is a geolithological chart of the AOI, which shows the lava tongue on which the ancient Appia road was built, and from which the basalt paving stones of the road were quarried. The majority of the surrounding geolithology is also volcanic and comprises pyroclastic deposits, including tuff [63]. Figure 22 shows the agropedology of the area, which consists of soils of class 1, 2 and 3. The limitations of the class 2 and 3 soils are mainly due to stoniness, shallow depth, poor texture or chemistry [69]. Figure 23 is a land use map of the area, with particular attention given to vegetation classes. Most of the AOI is taken up by arable land [64].

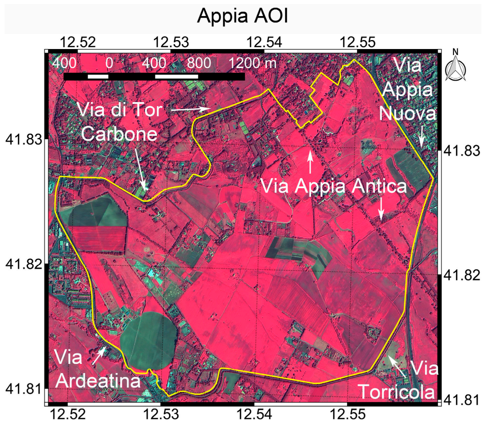

Figure 20. Kompsat-2 image of the Appia AOI (shown in yellow polygon) acquired on 21 April 2011, pansharpened to 1 m spatial resolution. False colour composite of NIR, R and G displayed as R, G and B respectively. Kompsat-2 data provided by the European Space Agency.

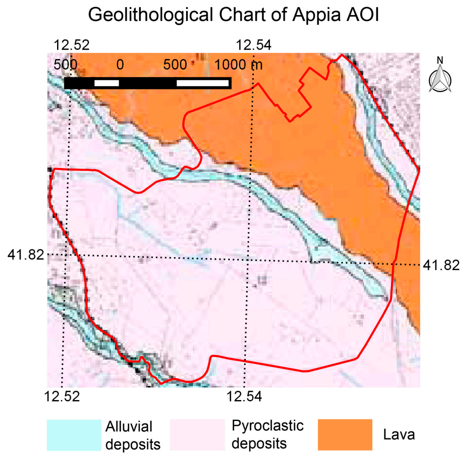

Figure 21. Geolithological chart of Appia AOI (shown in red polygon), last updated in 2007. Copyright: Comune di Roma [63].

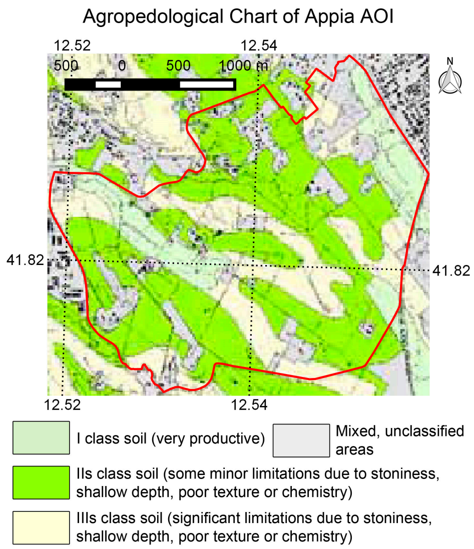

Figure 22. Agropedological chart of Appia AOI (shown in red polygon), last updated in 2007. Copyright: Comune di Roma [73].

The archaeology of the area is dominated by the Appian Way, the construction of which began in 312 BC [45,74]. Many structures were built in proximity to the road in antiquity, particularly tombs, but also inns, workshops and villas [45,74]. The AOI was chosen by the Mapping the Via Appia project due to its lack of modern development and the abundance of structures that were known to exist here in antiquity, and many of which are no longer present on the surface. These structures have been identified in various ancient sources: These include maps, such as from Carlo Labruzzi (1748–1817); etchings, such as those of Giovanni Battista Piranesi (1720–1778), and other sources. Various prospection techniques have been applied in the area by the Mapping the Via Appia project, including geophysical prospection (magnetometry, georadar and resistivity), analyses of historical air-photos and satellite imagery, and excavation. The results of these have been inserted into a project GIS [45]. This GIS has been used as a source of comparison for the SAR analysis.

Analysis of the SAR data did not reveal any features which could be unequivocally associated with the presence of buried archaeological structures: neither in the filtered σ^0 backscatter, nor in the coherence time series. The coherence time series was characterized throughout by low coherence, which inhibited InSAR or SBAS DEM generation.

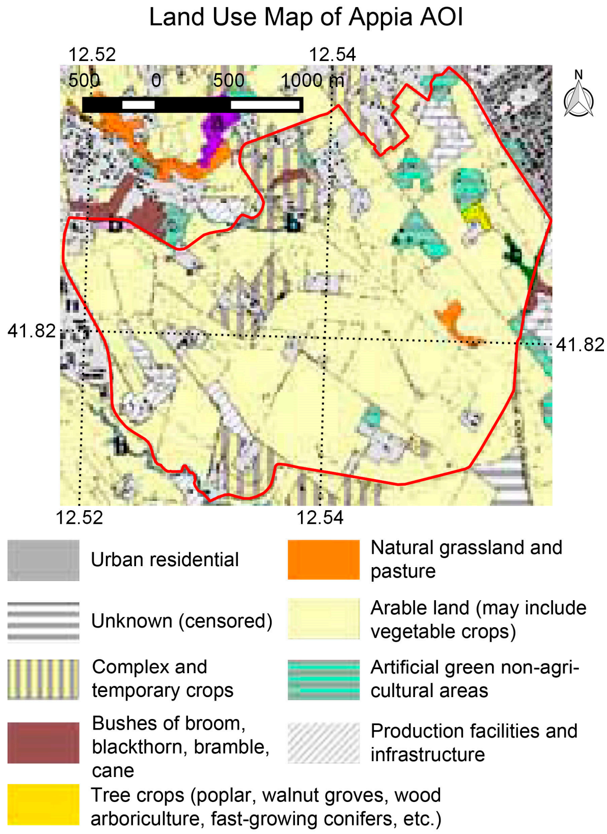

Figure 23. Land use map of Appia AOI (shown in red polygon), last updated in 2007, courtesy of the Comune di Roma [64].

4.4. Prenestina

The AOI of Prenestina comprises an isolated rural area situated south of the modern Via Prenestina, and between the urban areas of Prato Fiorito (to the east), Torre Gaia (to the south) and Torre Angela (to the west) (see Figure 24). Most of the AOI is occupied by arable fields of non-irrigated crops [64] (see Figure 25). The topography throughout the area is undulating. The soil is mainly of class 3. Its suitability for cultivation may be hindered by stoniness, shallow depth, poor texture or inferior chemical composition [69] (see Figure 26). The substrate is mainly pyroclastic, from the Albano volcano district, with some alluvial material in the valleys [63] (see Figure 27). This is one of the two largest AOIs (together with the Appia).

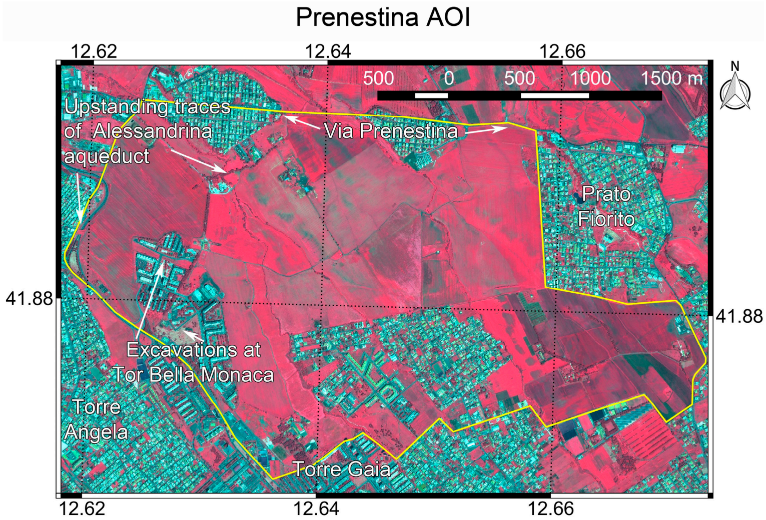

Figure 24. Pleiades image of the Prenestina AOI (shown in yellow polygon), acquired on 20 April 2014, pan-sharpened to 0.5 m spatial resolution and displayed as a false colour composite of NIR, R and G displayed as R, G and B.

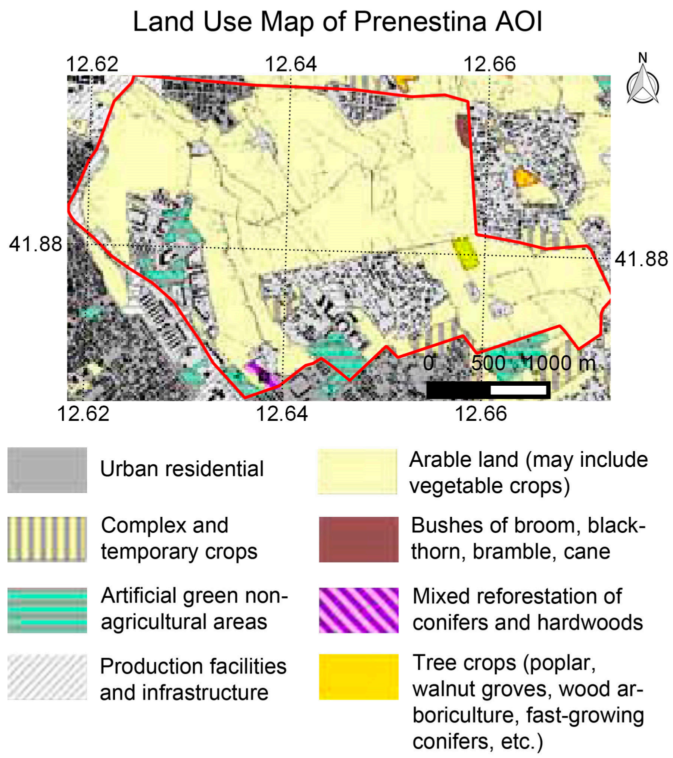

Figure 25. Land use map of Prenestina AOI (shown in red polygon), last updated in 2007. Copyright: Comune di Roma [64].

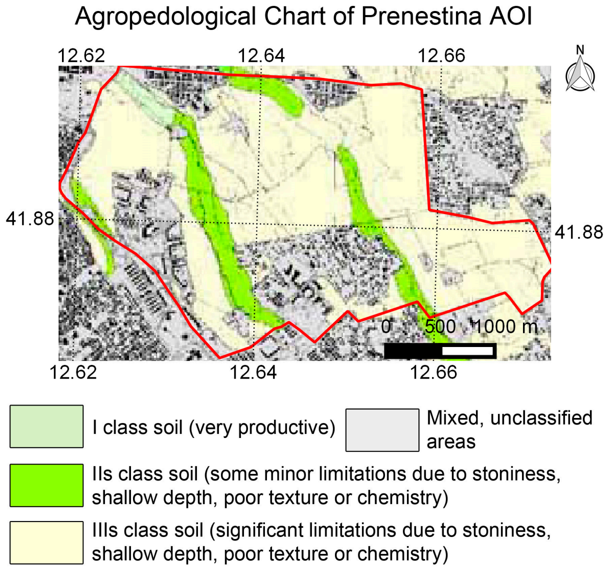

Figure 26. Agropedological chart of Prenestina AOI (shown in red polygon), last updated in 2007. Copyright: Comune di Roma [73].

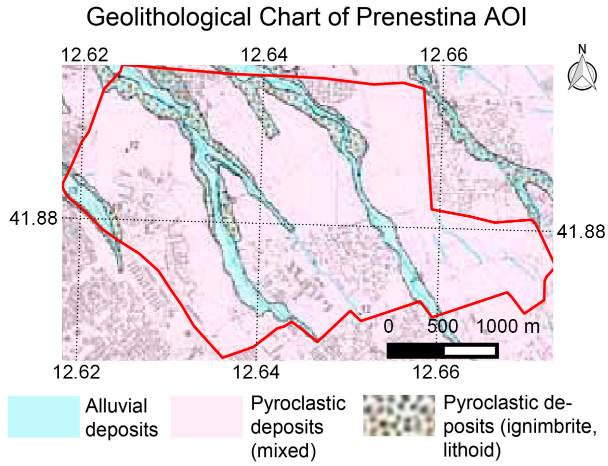

Figure 27. Geolithological chart of Prenestina AOI (shown in red polygon), last updated in 2007. Copyright: Comune di Roma [63].

The AOI lies approximately half way between the ancient cities of Rome and Gabii. It was traversed in antiquity by a number of Roman roads, including, amongst others, the Via Gabina, which then became the Via Prenestina. The Alessandrina aqueduct also crossed the area. Numerous other archaeological structures have been, to varying degrees of accuracy, identified in the area, including villas, tombs, wells and cisterns, and even small settlements [46]. A few structures have been excavated in the course of urban development. During the construction of Tor Bella Monaca in the 1980's, a part of the Via Gabina was excavated, revealing basalt paving stones. Part of the bath complex of a villa, in use from the fourth century BC, was also excavated, and the remains of a portico belonging to a Roman farmhouse [75]. Some structures are still upstanding, including some of the arches of the Alessandrina aqueduct. Most of the AOI has been un-touched by excavation and many archaeological features have been interpreted from scarce fragments of material at the surface following ploughing, such as ceramic, brick and stone [46].

The area in which the AOI is situated has, since the late 1950's, seen rapid and extensive urban development as a vast expansion of suburban Rome, as a result of which many archaeological sites have been destroyed [46]. The fast pace of development stimulated Lorenzo Quilici, in 1969, to begin a massive archaeological survey of an area of just over 10 × 10 km surrounding, and including, the AOI. This survey reports on the results of field walking, air photo interpretation and excavation, wherever these were undertaken. It provides a comprehensive description of all finds, including photos. It summarises the results of previous research in the area, such as that carried out by Pietro Rosa, Rodolfo Lanciani, Thomas Ashby and Jean Coste [46]. The 938 page volume was published in 1974, and this is the source used to validate archaeological residues identified in the SAR imagery of the area.

Over this AOI, archaeological residues were identified in all three SAR product types, and in both the Stripmap and Spotlight data. Results are reported here only of the Spotlight data processing given that the residues are generally clearer and more often present in all the product types of the Spotlight times series. This is probably due to the enhanced resolution, and the availability of 1-day as well as 16-day InSAR pairs.

Figure 28 shows one of the CSK Spotlight filtered σ^0 backscatter images, acquired on 25 July 2010. Figure 29 shows one of the Spotlight coherence images, derived from the InSAR couple acquired on 9 and 25 July 2010 (16 day temporal baseline). Figure 30 shows the Spotlight SBAS DEM. Figure 31 shows the subset covering the AOI of the map showing all the archaeological structures documented by Quilici, 1974 [46]. Figure 32 shows a Pleiades image over the AOI acquired on 20 April 2014 as a colour composite of NIR, R and G displayed respectively as R, G and B.

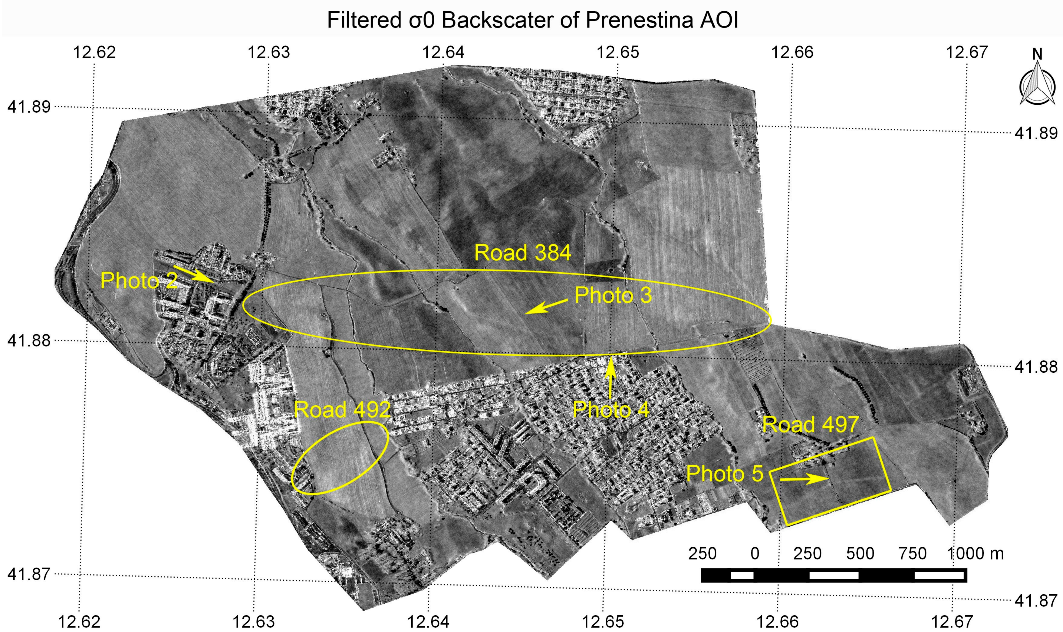

Figure 28. Image of filtered σ^0 backscatter over the Prenestina AOI acquired on 25 July 2010. Annotations in yellow show the locations of residues and the locations and directions from which photographs were acquired on the ground. COSMO SkyMed data provided by the Italian Space Agency.

On each of Figures 28–32 archaeological residues are highlighted in yellow. These are named according to their catalogue number in the archaeological chart of Quilici [46]. Their clarity differs between the various SAR products. The residues are all of roads. Most other structures recorded in this area in Quilici [46] have been interpreted from scant surface fragments, and they may not have a coherent form.

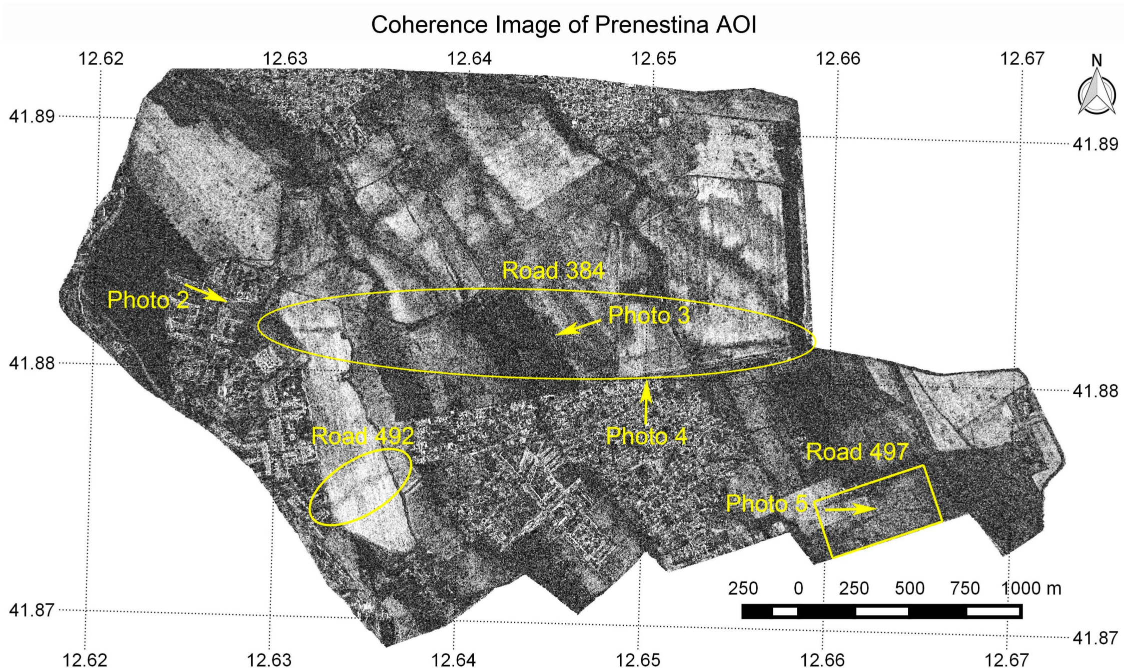

Figure 29. Coherence image from CSK Spotlight InSAR pair acquired on 9 and 25 July 2010 over the Prenestina AOI. Annotations in yellow show the locations of residues and the locations and directions from which photographs were acquired on the ground. COSMO SkyMed data provided by the Italian Space Agency.

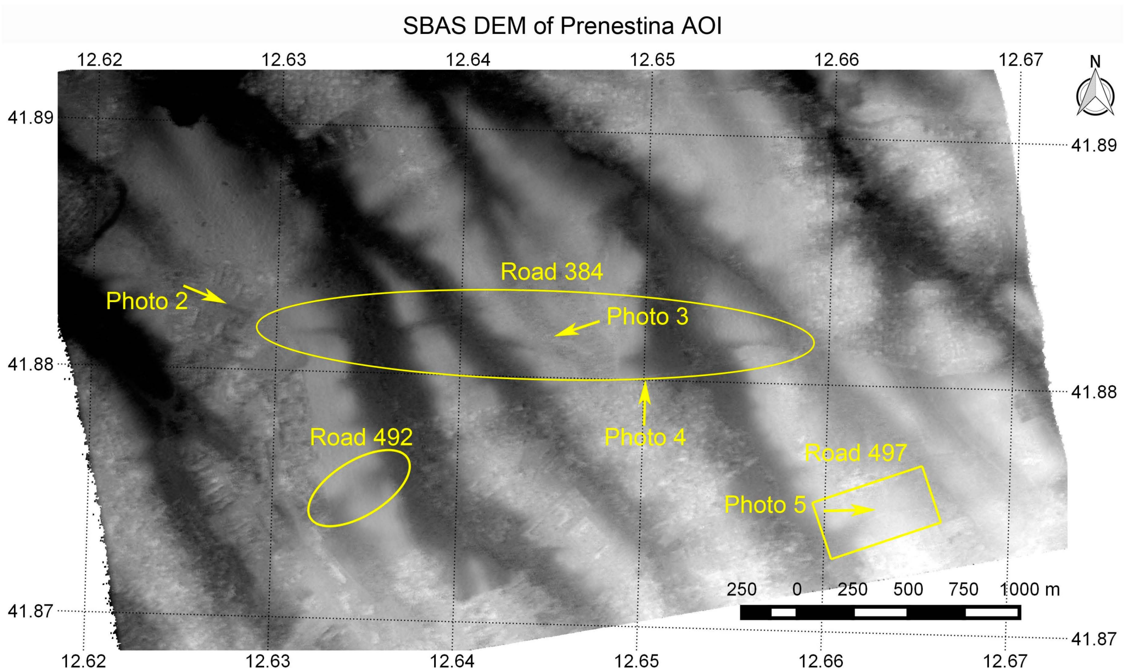

Figure 30. SBAS DEM produced from CSK Spotlight imagery over the Prenestina AOI. Annotations in yellow show the locations of residues and the locations and directions from which photographs were acquired on the ground. COSMO SkyMed data provided by the Italian Space Agency.

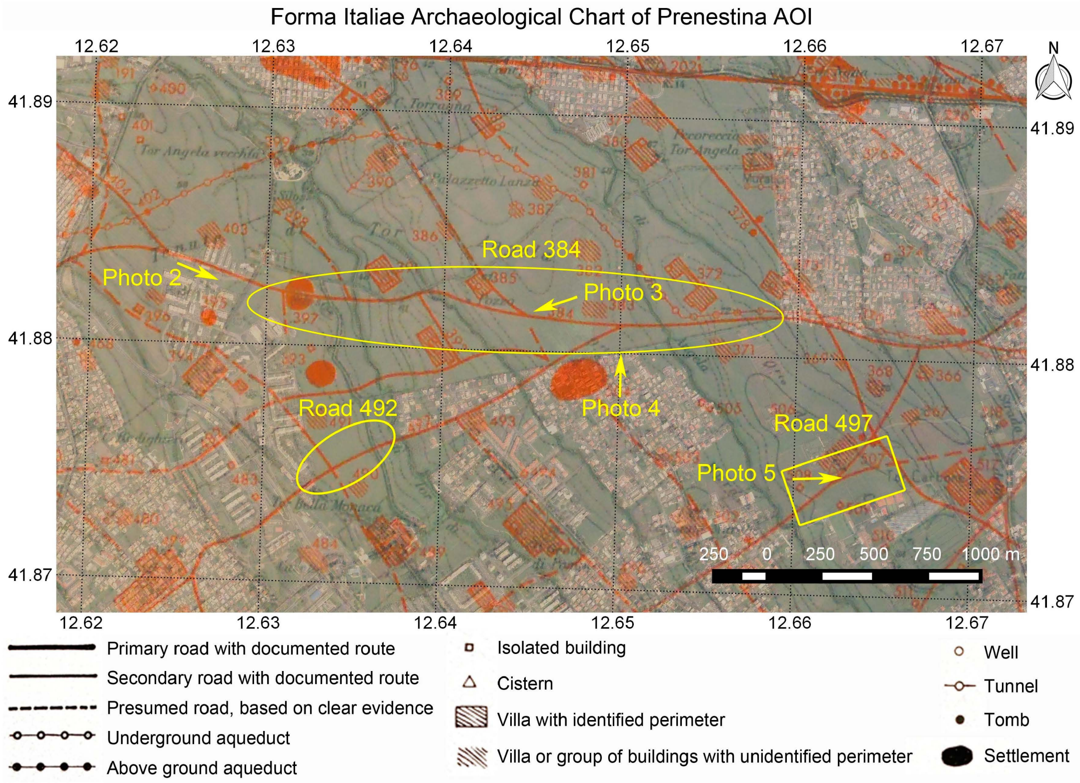

Figure 31. Subset of archaeological chart over the Prenestina AOI taken from Quilici, 1974 [46] and published as part of the Forma Italiae series. Annotations in red show documented archaeological structures, annotations in yellow show the locations of residues and the locations and directions from which photographs were acquired on the ground.

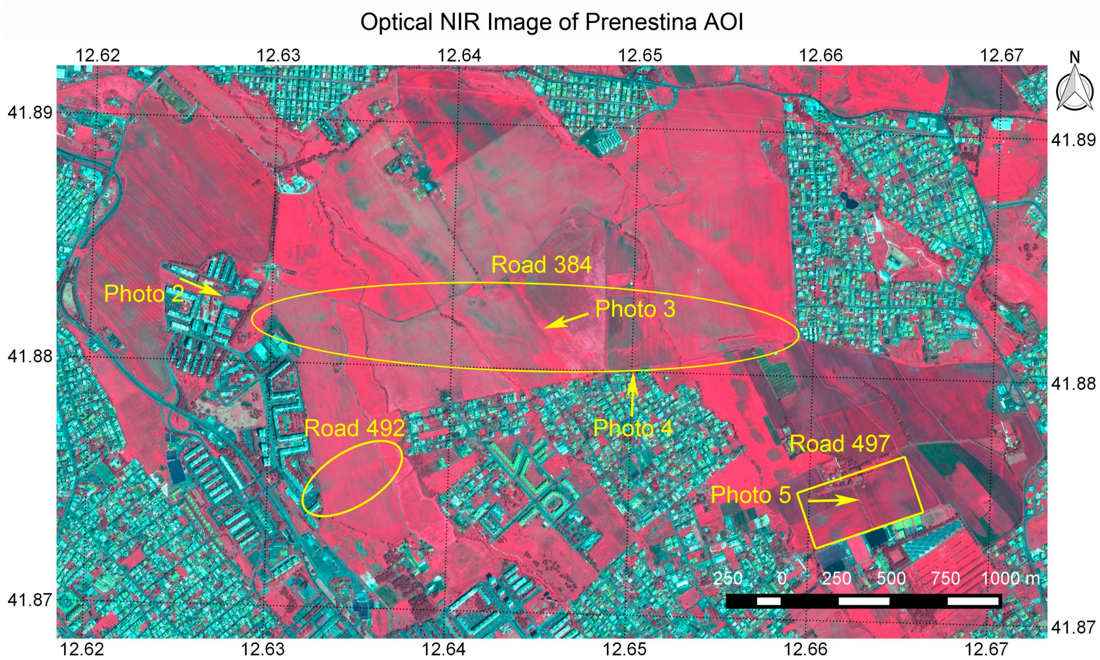

Figure 32. Pleiades image acquired on 20 April 2014 over the Prenestina AOI, pan-sharpened to 0.5 m spatial resolution. NIR, R and G displayed as R, G and B respectively. Pleiades data provided by the European Space Agency.

4.4.1. Road 384

In the archaeological chart of Quilici, 1974 [46], a road has been recorded that traversed the AOI horizontally, to the south of, and parallel to, the modern Via Prenestina. The road (with catalogue number 384) was also identified in parts by scholars such as Rodolfo Lanciani and Thomas Ashby. Traces of it are visible in air photos as crop marks [46]. A part has been excavated at Tor Bella Monaca Figure 33, revealing the basalt paving stones of two phases of development. This excavated part continues for no longer than around 245 m. Elsewhere in the AOI the only traces at the surface are topographic. In some cases as a very narrow trough Figure 34, and in others as a wider valley Figure 35. The road has been identified as the Via Gabina, which then became the Via Prenestina [75]. However, for consistency, here it will be referred to by its catalogue number in Quilici as "Road 384".

Photo 2: Excavated Part of Road 384

Figure 33. Photograph acquired of the part of Road 384 that was excavated during the construction of Tor Bella Monaca in the 1980's. Two phases of development can be seen from the two layers of paving and different widths. The photograph was acquired on 16 March 2013 at 18:27 CET.

Photo 3: Visible Trace of Road 384

Figure 34. Photograph acquired of the location of a part of Road 384, evident as a narrow trough in the center of a broad valley. The photograph was acquired on 16 March 2013 at 17:01 CET.

This feature is visible in all the SAR product types: in the filtered σ^0 backscatter images the centre is most visible (where there is a narrow trough), in the coherence images the parts of the road that continue along wider valleys appear clearest, while in the DEM, most sections are visible. It is likely that the topography itself is the cause of the residues in all SAR products. The filtered σ^0 backscatter is sensitive to the narrow trough probably due to its geometry, the sides of which possibly act as corner reflectors. This would explain why this segment of the road is visible in all the images of filtered σ^0 backscatter, as the geometry is less ephemeral than a crop or soil mark. The coherence residue, which is always distinguished by lower coherence over the feature with respect to surrounding areas, is likely due to increased crop growth at the bottom of the wider valleys where water would collect. The best example of the coherence residue is in the 9 and 25 July 2010 pair (16 day temporal baseline).

Photo 4: Visible Trace of Road 384

Figure 35. Photograph acquired of the location of a part of Road 384, situated in the center of the broad valley visible in the photograph. The photograph was acquired on 6 October 2015 at 12:36 CET.

4.4.2. Road 492

This road is recorded in Quilici [46] as having been identified by Pietro Rosa in the late 19th century [76] as surface remains in open fields which are now occupied by modern urban development. The road was also observed as crop or soil marks in air photos, and pieces of stone paving, brought to the surface by ploughing, can be found occasionally throughout the course of the road [46]. In this short stretch between the urban areas of Valle Fiorita and Tor Bella Monaca, it appears clearly on the DEM and in the same coherence images in which the residue of Road 384 appears as it crosses the same field. It is much less evident in the images of filtered σ^0 backscatter.

4.4.3. Road 497

This road, which connected the settlement of Osteria dell'Osa with the Via Casilina, was still in use in the first decades of the 20th century. The segment of this road highlighted in Figures 28–32 shows on the archaeological chart of Quilici (Figure 31) as a continuous line followed by a dashed line (after a fork in the road). The line becomes dashed as no physical traces remained of the segment at the time the archaeological chart was published. However, based on evidence elsewhere along its course, it was suspected to have continued along the route of the dashed line [46].

Parts of this road are visible in some of the images of filtered σ^0 backscatter (see Figure 36a), and coherence (see Figure 36b). Along the dashed line there is no longer any topographic trace in the DEM (see Figure 36c). On 6 October 2015 a UAV was flown over this part of the feature and a very high resolution photogrammetric DEM was produced, with a spatial resolution of 12 × 12 centimeters (see Figure 36d). In this DEM a trace of the road is visible where it is suspected to continue. It is also visible in the UAV orthophoto that was used as input to the DEM (see Figure 36e). It is partly visible in a Pleiades image acquired on 20 April 2014, displayed as a colour composite of NIR, R and G displayed respectively as R, G and B in Figure 36f. A subset of this area in the archaeological chart of Quilici is shown in Figure 36g. No topographic or other traces are visible on the ground (see photo 5 in Figure 36h).

The archaeological chart of Quilici documents the presence of other roads, and a villa with unknown perimeter, in the same area as the segment of Road 497 discussed here (see Figure 36g). None of these have been identified in any of the imagery, SAR or optical. From extensive surface finds, the villa is thought to be at the centre of a vast archaeological area [46]. Perhaps the remains of these features are scattered, due to damage or looting, to the extent that they no longer have a coherent shape that may be detectable on remotely sensed imagery.

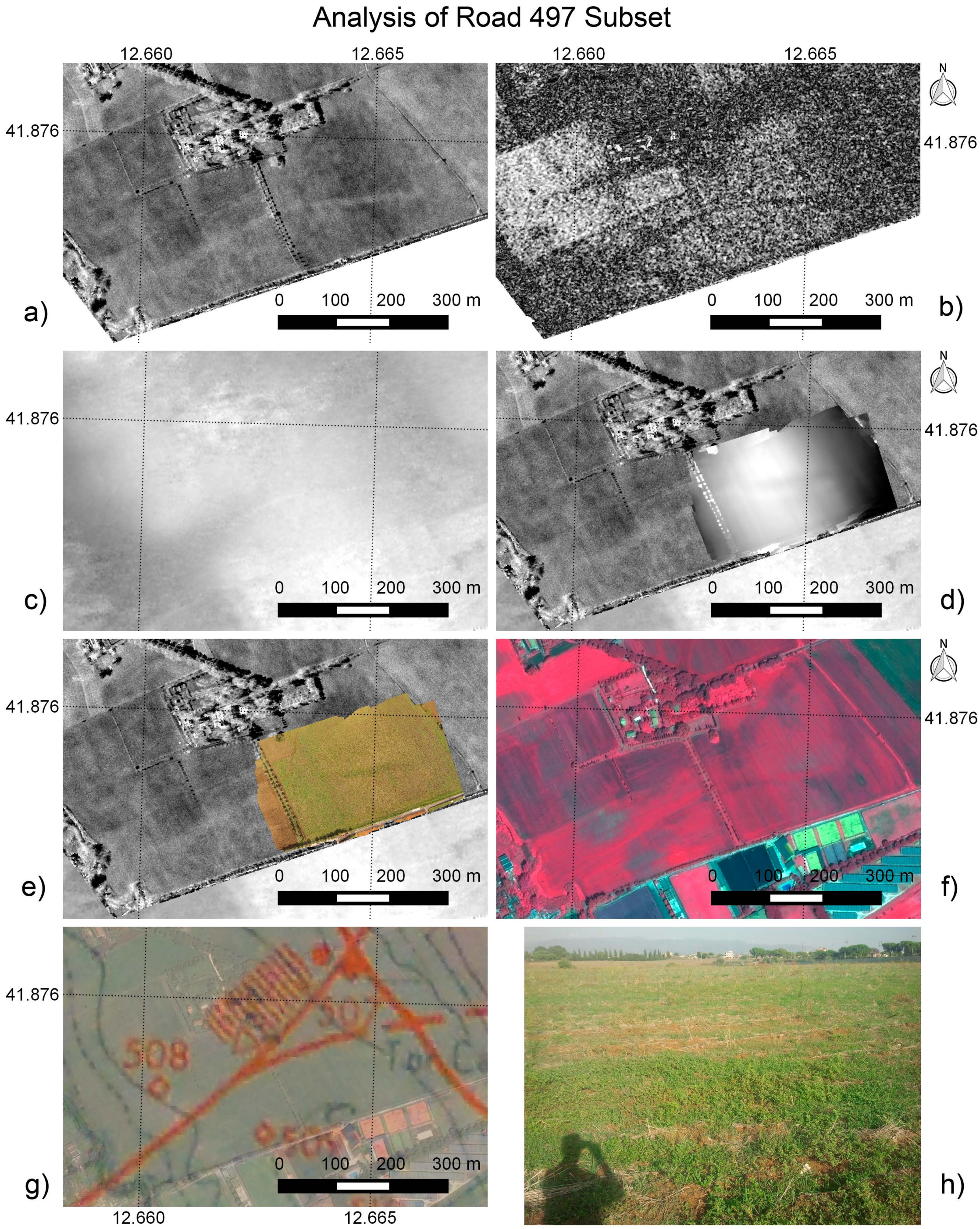

Figure 36. Subsets of Road 497, as shown in yellow rectangle in Figures 28–32: (**a**) CSK Spotlight image of filtered σ^0 backscatter, acquired on 25 July 2010; (**b**) CSK Spotlight coherence image with 16 day temporal baseline from image pairs acquired on 9 and 25 July 2010; (**c**) SBAS DEM produced from CSK Spotlight time series; (**d**) DEM derived from UAV photogrammetric imagery acquired on 6 October 2015, overlain on imagery in part (**a**); (**e**) Orthophoto acquired by UAV on 6 October 2015, overlain on imagery in part (**a**); (**f**) Pleiades image acquired on 20 April 2014, pan-sharpened to 0.5 m spatial resolution. NIR, R and G displayed as R, G and B respectively; (**g**) Archaeological chart of Quilici, 1974 [46] overlain on true colour Pleiades image acquired on 20 April 2014; (**h**) Photo 5. Acquired on 19 September 2015 at 17:03 CET. The location and direction from which the photo was taken is shown in Figures 28–32. COSMO SkyMed data provided by the Italian Space Agency. Pleiades data provided by the European Space Agency.

4.4.4. Prenestina Features Analysis

The contrast of the archaeological residues in the various SAR images were quantified and compared over time. They were also correlated with PSMD and coherence, as described in Section 3. Figure 37a shows the MRD subsets over a western part (green) and an eastern part (red) of Road 384 overlain on one of the clearest images on which these residues appear: the coherence image from the CSK Spotlight pair acquired on 9 and 25 July 2010. Figure 37b shows the MRD subsets over Road 497 overlain on the clearest image on which this residue appears: the CSK Spotlight image of filtered σ^0 backscatter, acquired on 25 July 2010. Figure 38a shows the areas where profile plots were produced from the Spotlight SBAS DEM of the topographic residues of Road 384. Figure 38b shows the area where a profile plot was produced from the UAV DEM of the topographic residue of Road 497.

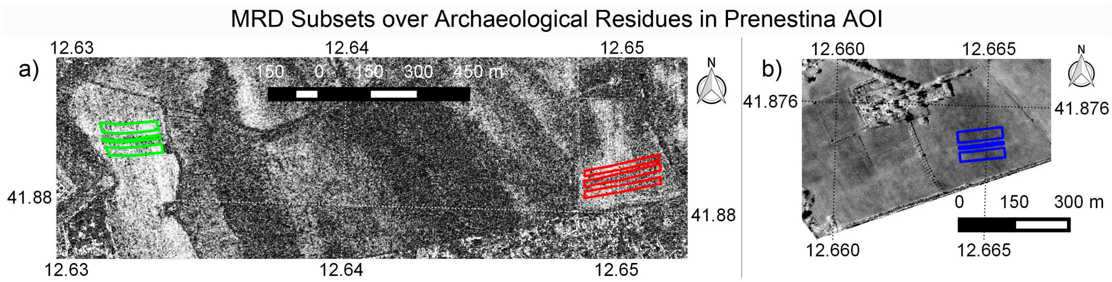

Figure 37. Subset areas shown as coloured polygons over and outside of residues used for MRD contrast analysis: (**a**) Green and red polygons over and outside of residues of Road 384. Polygons are overlain on CSK Spotlight coherence image from InSAR pair acquired on 9 and 25 July 2010; (**b**) Blue polygons over and outside of residue of Road 497. Polygons are overlain on σ^0 image acquired on 25 July 2010. COSMO SkyMed data provided by the Italian Space Agency.

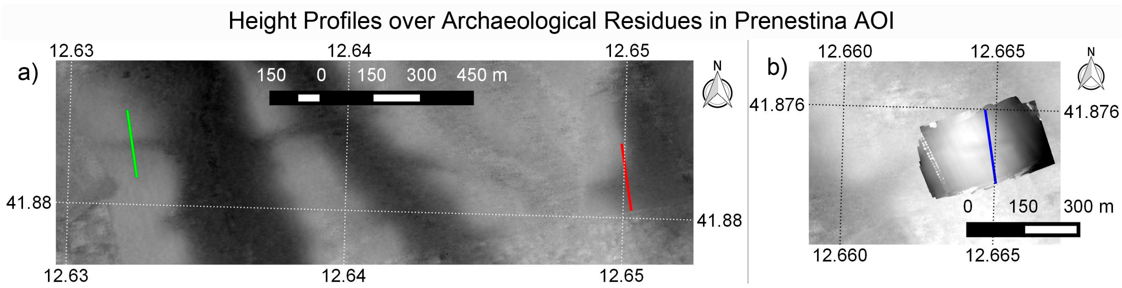

Figure 38. Profiles over residues in Prenestina AOI. Height measurements along the profiles in the various DEMs are plotted in Figure 43. (**a**) Profiles (in green and red) over residues of Road 384 overlain on SBAS DEM produced from CSK Spotlight time series. COSMO SkyMed data provided by the Italian Space Agney; (**b**) Profile (in blue) of residue of Road 497 overlain on DEM derived from UAV photogrammetry.

The reason for selecting two areas for MRD calculation along Road 384 is that they are both in different fields and the similarity in the contrast of the two archaeological residues are not the same in all images. No analysis was done of Road 492 due to the fact that the archaeological residue over the western part of Road 384 lies in the same field as the residue of road 492, and the difference in the clarity of each is the same for every image (the residue of the western part of Road 384 is always a little clearer than that of Road 492).

Figure 39 compares the clarity of each of the archaeological residues in each of the Spotlight SAR products (filtered σ^0 backscatter, 1 and 16 day coherence), plotted over time and with PSMD. The DEM is not included as this was calculated using the entire time series. The chart shows that the coherence residues over the eastern and western parts of Road 384 and over Road 497 all have similar contrast changes over time. The clearest coherence residues are in the 16 day coherence imagery from July 2010, in particular for the western part of Road 384. The σ^0 residues over the three features do not vary consistently over time as do the coherence residues. However, in the case of the σ^0 residues over Road 384, the residues seem more to be due to a geometric effect of the topography, particularly in the central part (the eastern part revealing no significant residue, while the western part a little more, but still not varying significantly over time). The σ^0 residue over Road 497 on the other hand may more likely be a crop or soil mark than a geometric effect of the topography, and the peak residue contrast coincides with the peak coherence contrast in July 2010.

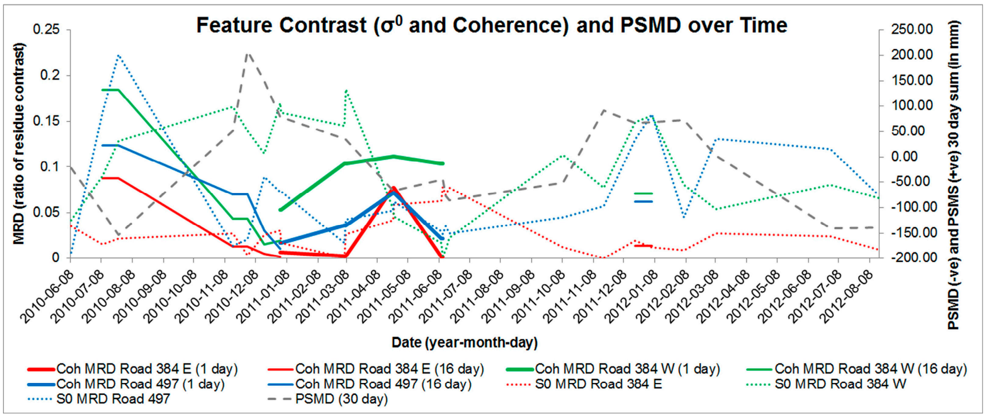

Figure 39. Graph showing clarity (contrast) of the archaeological residues in Prenestina: eastern part of Road 384 in red, western part of Road 384 in green and Road 497 in blue. Residues in the filtered σ^0 images are shown as dotted lines, in the 16-day coherence images as continuous lines, and in the 1-day coherence images as bold continuous lines. The clarity of residues is quantified as a ratio (MRD). PSMD and PSMS plotted as a grey dashed line. Negative values correspond to high PSMD (dry conditions), while positive values correspond to high PSMS (wet conditions).

There does not appear to be any correlation between the σ^0 residues and PSMD, although the time of peak visibility of the σ^0 residue over Road 497 coincides with the time of greatest soil moisture deficit. This supports the argument that the σ^0 residue over Road 497 may be a crop mark, given that archaeological crop marks caused by differential crop growth often occur at times of drought (see Section 1.1). In contrast, there does seem to be some correlation between PSMD and the coherence residues, which appear with greater contrast at times of high soil moisture deficit, and less with high soil moisture surplus. This also supports the argument that the coherence residues are crop marks. The fact that all the coherence residues are due to lower coherence than surrounding areas leads further to interpret the features as positive crop marks.

Figure 40 compares the contrast of the three coherence residues with the coherence of each respective residue (calculated over the subsets which include the residues only). Interestingly, for the 16 day coherences there seems to be a proportional relationship between residue contrast and coherence, while over the 1 day coherences there appears to be an inversely proportional relationship. Given that coherence is entirely lost over the vegetated areas in most of the 16 day coherence images, it is not surprising that low residue contrast coincides generally with low coherence. However, the coherence is never entirely lost over the vegetated areas in any of the 1 day coherence images, as a consequence of which the relationship has more significance. The lower coherence may be a result of higher vegetation and a greater sensitivity to differential vegetation growth. The lower coherence may of course be due to other factors, such as rainfall, but the high contrast in 1-day coherence residues also coincide with greater soil moisture deficit (see Figure 39).

Figure 41 compares the contrast of the σ^0 residues over time with coherence over the residues. No particular correlation is observable between the residues over Road 384 and their coherences, but as stated above, these residues are likely to be geometric and due to a lesser extent to environmental or vegetation factors. Over the σ^0 residue of Road 497, while there is little observable correlation in the absolute values (exacerbated by the difference between 1 and 16 day coherences), there is nonetheless some similarity in their patterns over time, with highest coherence observed at times of highest σ^0 residue contrast.

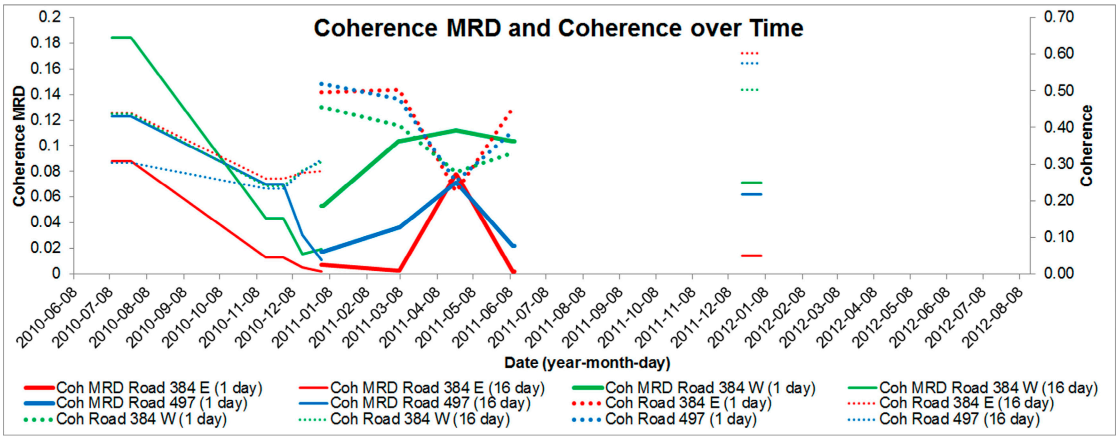

Figure 40. Graph showing contrast of coherence residues, as described in Figure 39, and coherence over each residue (in dotted lines). The coherence values are provided both for the master and the slaves of InSAR pairs. Where a master is also a slave, it takes the value of the slave.

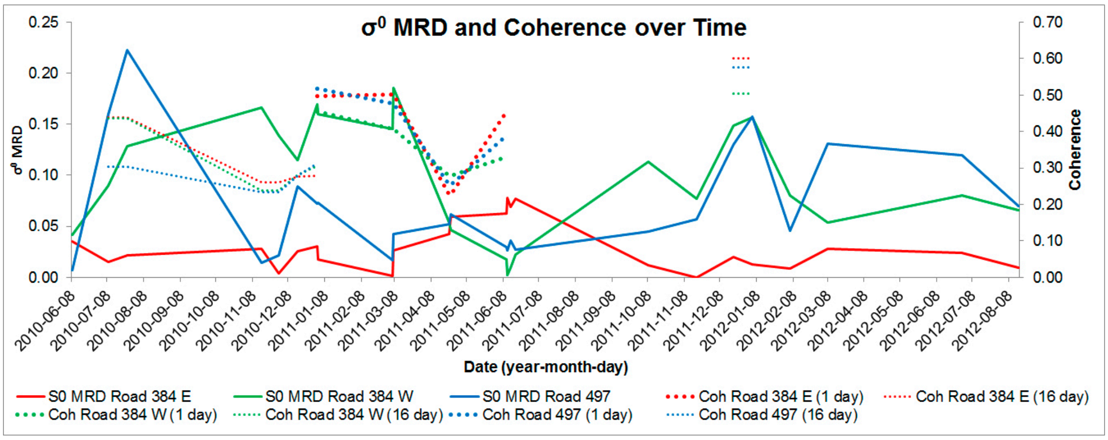

Figure 41. Graph showing contrast of σ^0 residues, as described in Figure 39, and coherence over each residue (in dotted lines). The coherence values are provided both for the master and the slaves of InSAR pairs. Where a master is also a slave, it takes the value of the slave.

Figure 42 compares the contrast of the σ^0 residue with the 1 and 16 day coherence residues of Road 497. Some correlation can be observed with the 16 day coherence residues, supporting the argument that these are manifestations of positive crop marks on both the σ^0 and coherence images. No significant correlation exists with the 1 day coherence residues, although residues were identified over Road 497 neither in the 1 day coherence images, nor in the σ^0 images on the dates of the 1-day coherence acquisitions.

Figure 43 shows the topographic profile of the eastern and western residues of Road 384 on the DEM derived from the SBAS processing using the Spotlight data, and the topographic profile of the residue of Road 497 on the DEM produced by optical UAV photogrammetry. The residues of Road 384 show clear valleys of differing widths. The residue of Road 497 shows a very slight topographic trace, but this is negligible compared to surrounding topography, and is not visible on the ground.

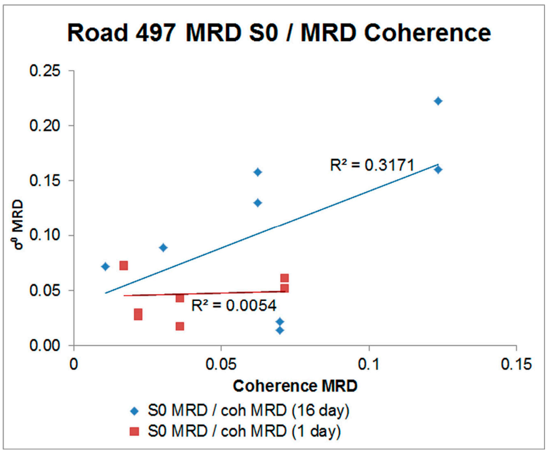

Figure 42. Graph showing clarity of σ^0 residue of Road 497, plotted against clarity of 16-day (blue) and 1-day (red) coherence residues of the same feature. Linear trend lines and R^2 values are shown in blue for the 16-day coherence/σ^0 plot, and red for the 1-day coherence/σ^0 plot. A better correlation can be seen for the 16-day coherence/σ^0 plot.

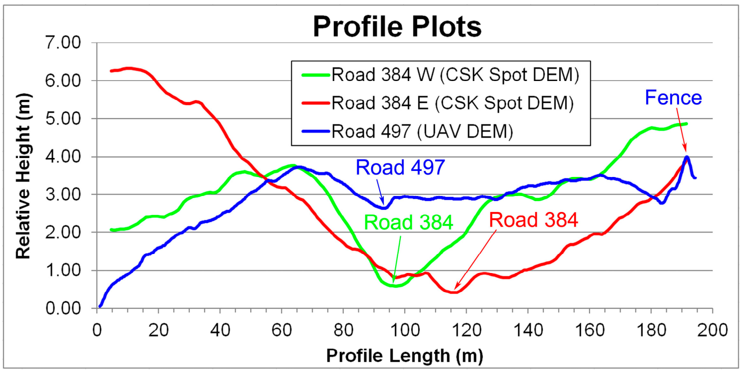

Figure 43. Graph showing height profiles over archaeological residues: western (green) and eastern (red) parts of Road 384, both taken from SBAS DEM derived from CSK Spotlight data, and Road 497 (blue), taken from DEM derived from UAV photogrammetry. Annotations for each profile are shown in their respective colours. The locations of the profiles are shown in Figure 38.

4.5. Salaria

The AOI of Salaria is the smallest AOI. It includes two fields of irrigated arable crops [64] traversed by the ancient Via Salaria 10 Roman miles from its origin [47]. The area is situated on the edge of the flat lands of the Tiber valley, north of the settlement of Settebagni and in between the modern Via Salaria (to the right) and the A1 "Roma Nord" motorway (see Figure 44). The substrate is alluvial [63] and the soils of the fields are of class 2, with only minor limitations for cultivation due to stoniness and excess water, either in the form of stagnant water in the soil or possible flooding [69].

The ancient Roman Via Salaria is believed to have been constructed as a paved road from the beginning of the third century BC [77]. No trace of the ancient Via Salaria is visible on the surface of the fields, but the line of the road has been identified as crop marks in optical air photos (e.g., by Quilici and Quilici Gigli in the 1970s [47]) and in optical satellite imagery (e.g., by Panu Hyppönen in 2014 [78]). In 1977, a cylindrical stone was found in the area, which is believed to be the 10th milestone. It was discovered at a depth of around 70 cm, during ploughing, at around kilometre 17.7 of the modern via Salaria [47,78]. The standard width of "viae publicae" (public roads) constructed from the third century BC was generally around 4.2 meters, which was sufficient to allow two way traffic [79], this corresponds with the width of crop marks over the road in the AOI.

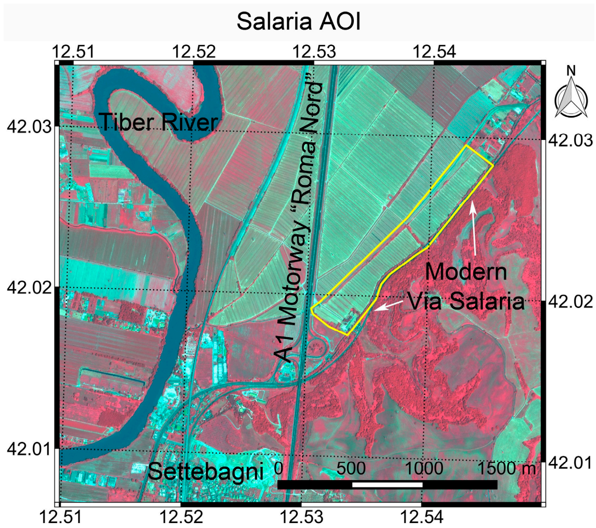

Figure 44. Pleiades image of the Salaria AOI (shown in yellow polygon) acquired on 22 May 2014, pansharpened to 0.5 m spatial resolution and displayed as a false colour composite of NIR, R and G respectively as R, G and B. Pleiades data provided by the European Space Agency.

Figure 45 is a Pleiades image of the Salaria AOI acquired on 22 May 2014 and displayed as a colour composite of NIR, R and G as R, G and B respectively. Figure 46 shows the AOI on a filtered σ^0 backscatter image acquired on 7 April 2013. This is the filtered σ^0 image on which the residue of the ancient Via Salaria appears clearest as a line of low backscatter traversing the field adjacent to the modern Via Salaria. All the residues on the filtered σ^0 images appear as areas of lower backscatter relative to surrounding areas. No residues were identified in any of the coherence images.

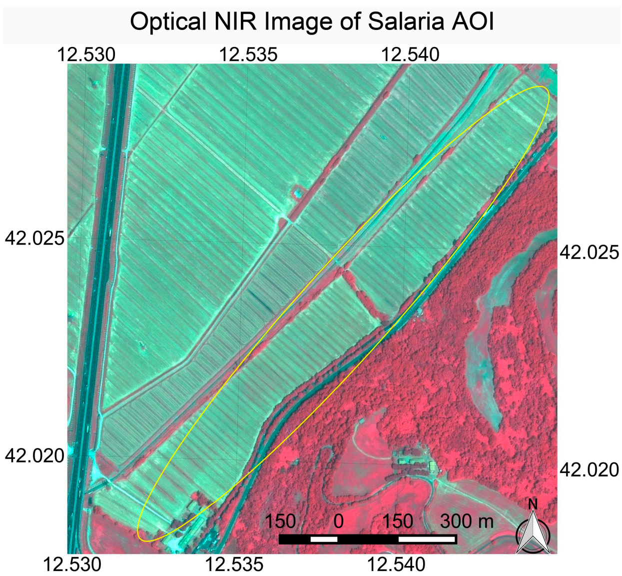

Figure 45. Pleiades image acquired on 22 May 2014 over the Salaria AOI, pan-sharpened to 0.5 m spatial resolution. NIR, R and G displayed as R, G and B respectively. Yellow ellipse shows location of the residue of the ancient Via Salaria. Pleiades data provided by the European Space Agency.

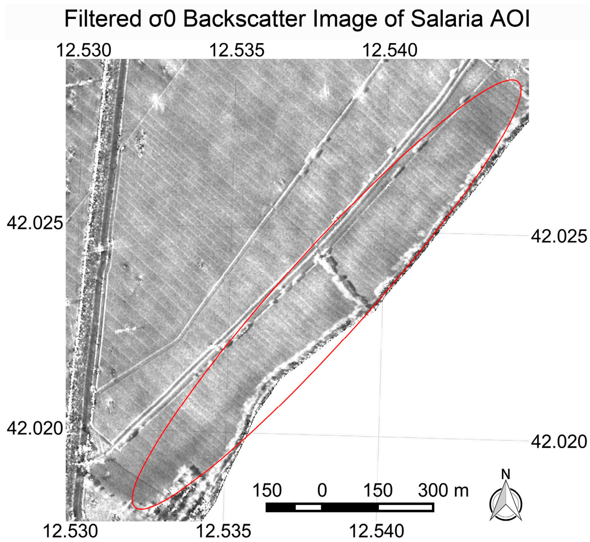

Figure 46. Image of filtered σ^0 backscatter over the Salaria AOI acquired on 7 April 2013. Red ellipse shows location of the residue of the ancient Via Salaria. COSMO SkyMed data provided by the Italian Space Agency.

Figure 47 shows the DEM produced from the image pair acquired on 10 and 26 August 2012. The result is very noisy given the low coherence, but the ancient Via Salaria can be seen very clearly as a slight topographic depression traversing the fields. This was one of the few image pairs from which it was possible to derive a DEM (albeit noisy) and the only one on which the Via Salaria is visible.

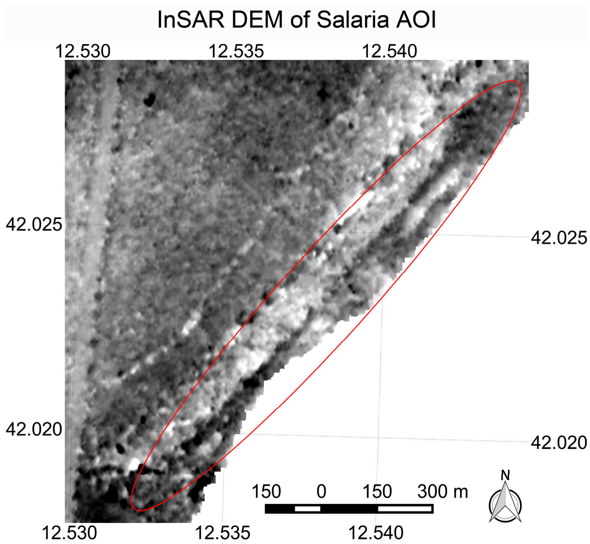

Figure 47. DEM over the Salaria AOI derived from InSAR using the CSK Stripmap image pair acquired on 10 and 26 August 2012. Red ellipse shows location of the residue of the ancient Via Salaria. The DEM is very noisy, but the residue of the ancient Via Salaria can clearly be seen.

Figure 48 is a photo acquired of the area on 1 October 2016. No topographic, or any other, trace of the ancient Via Salaria is visible. Figure 49 shows the best available example of the ancient Via Salaria as a straight negative crop mark surrounded by positive crop marks, in an optical image available on Google Earth, acquired on 11 September 2009. The location and direction from which the photo in Figure 48 was acquired is shown as a yellow arrow on this image.

Figure 48. Photo 6 acquired at the location of the residue of the ancient Via Salaria (see Figure 49 for location and direction of photo). Photo acquired on 1 October 2016 at 17:14 CET. On this date, no trace is visible of the archaeological feature on the ground.

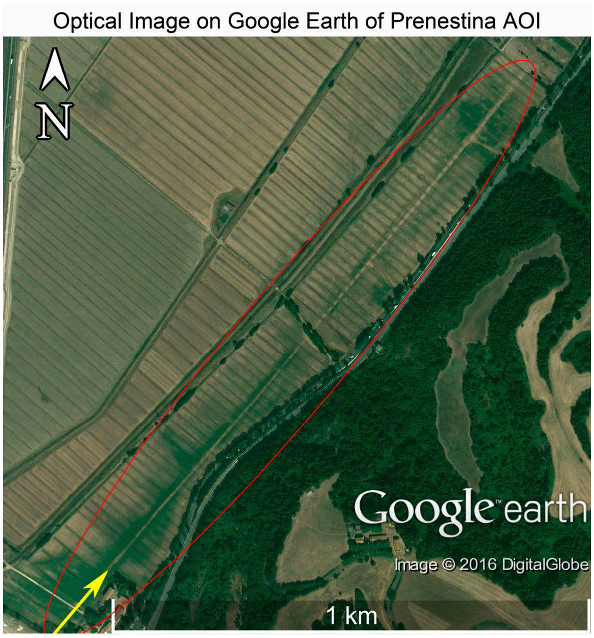

Figure 49. Optical image available on Google Earth, acquired on 11 September 2009. The ancient Via Salaria (highlighted by the red ellipse) is clearly visible as a negative crop mark with positive crop marks on either side along the southern part of the feature. Yellow arrow shows location and direction in which photo 6 was acquired (Figure 48). Courtesey of Google Earth.

Salaria Features Analysis

Figure 50 shows the subset areas over the ancient Via Salaria, and on either side of it, which were used to quantify the residue contrast in each of the σ^0 backscatter images. Figure 51 compares the σ^0 residue contrast of the Via Salaria over time and with PSMD. The graph shows no clear correspondence between PSMD and σ^0 residue contrast, although the times of highest contrast coincide with a period of high PSMS, which is not characteristic of crop marks.

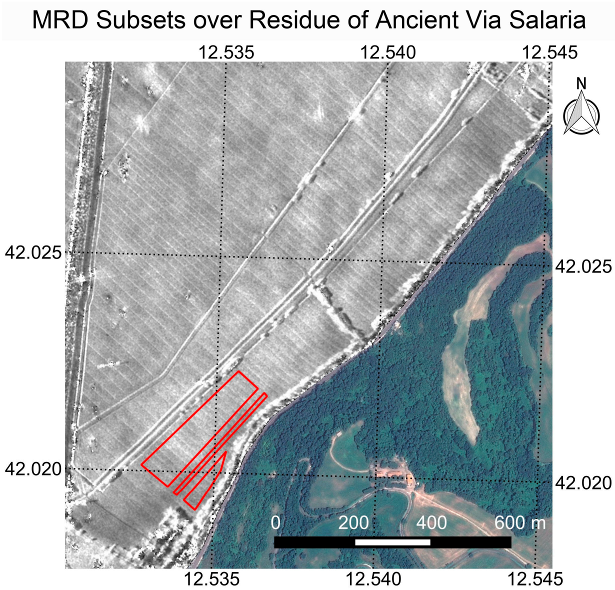

Figure 50. Subset areas used for MRD contrast analysis shown as red polygons over and outside of the Via Prenestina residue. Polygons are overlain on the image of filtered σ^0 backscatter acquired on 7 April 2013 and Pleiades image acquired on 22 May 2014. COSMO SkyMed data provided by the Italian Space Agency. Pleiades data provided by the European Space Agency.

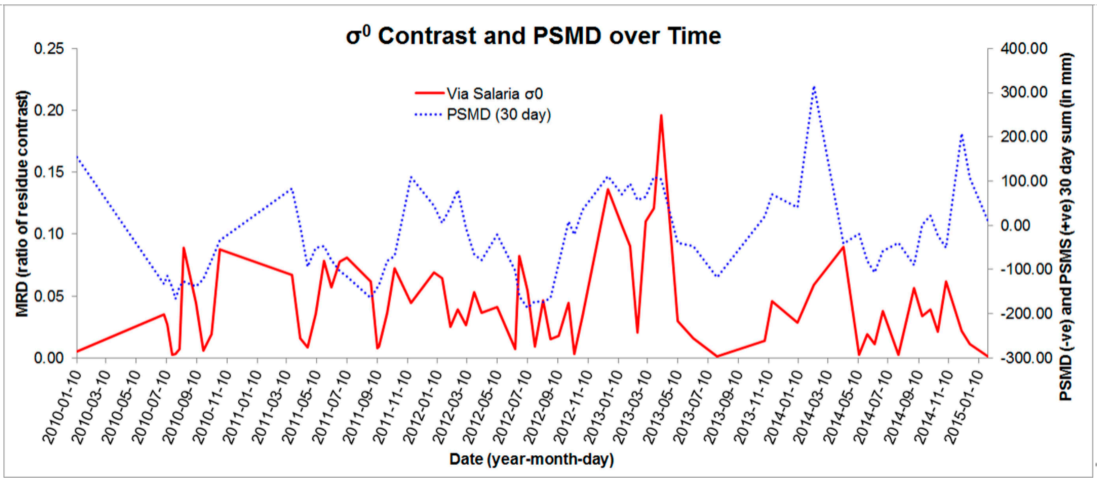

Figure 51. Graph showing clarity (contrast) of the residue of the ancient Via Salaria (in red), plotted over time and with PSMD (blue dotted line). The clarity of residues is quantified as a ratio (MRD). For the PSMD, negative values correspond to high PSMD (dry conditions), while positive values correspond to high PSMS (wet conditions).

Figure 52 shows σ^0 residue contrast with residue coherence. Throughout most of the time series there is no clear σ^0 residue contrast and coherence is consistently low. At the time of greatest σ^0 residue contrast, the coherence is at the same low value as throughout most of the time period.

Given that the σ^0 residues appear as areas of lower relative backscatter, and given the low coherence in all images, it is likely that these residues are manifestations of negative crop marks, as is the case with the image on Google Earth. The presence of the topographic anomaly on the DEM indicates that there is still a slight topographic trace of the road. The photograph of the location of the residue on the ground shows that this is not visible at the surface (at least not at the time the photo was acquired). The negative crop mark along the buried road in the image on Google Earth is perhaps due to paving stones beneath the ground hindering crop growth. The positive crop marks on either side of the road in the same image may correspond with ancient drainage channels, but their broad and irregular nature, and the fact that they are mainly in the southern part of the road, suggests that they may instead be due to the accumulation of water within the slight valley causing enhanced crop growth where this is not hindered by the ancient road. The presence of this slight valley may also be the reason why the σ^0 residue appears more clearly at a time of high PSMS, as high PSMS perhaps enhances the difference between abundant vegetation growth in the valley with stunted growth over the buried road. Although this is in contrast with the appearance of the residue in the available optical imagery of the area, on which it appears mainly in the hot summer months of July, August and early September, when the vegetation is parched. However, the appearance of crop marks in optical images is a result of colour differences, which is not the case for SAR.

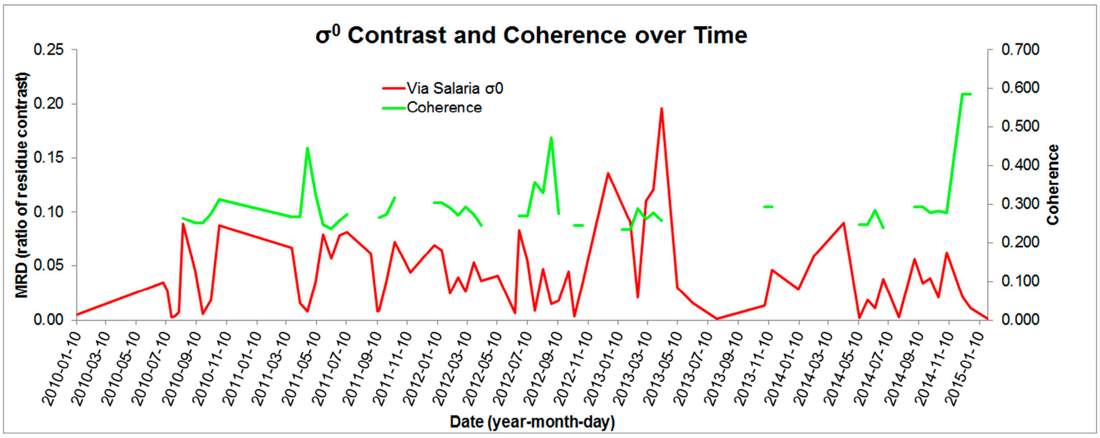

Figure 52. Graph showing clarity (contrast) of the residue of the ancient Via Salaria (in red), plotted over time and with residue coherence (in green). The clarity of residues is quantified as a ratio (MRD).

The CSK Stripmap images used to produce the DEM were acquired on 10 and 26 August 2012. This does not coincide with high contrast of residues on the σ^0 backscatter, but it does coincide with high PSMD and high coherence. Perhaps the stunted and parched vegetation is less likely to contribute to temporal decorrelation than healthy, abundant growth. This may also be a time for the emergence of crop marks, as confirmed in the available optical images. It may be therefore that the topographic anomaly is due to differential crop growth. Perhaps not as enhanced as at other times, but possible to measure with InSAR due to the higher coherence.

4.6. Veii

The AOI of Veii is situated in the rolling countryside between the Tiber valley and the Sabatino volcano district, on a raised plateau of tuff from the pyroclastic deposits of the Sabatino volcanic eruptions [63]. It is located to the east of the small settlement of Isola Farnese (see Figure 53). The landscape comprises arable fields and permanent pasture [64]. The soils include class 1 (very productive) to class 2 (some minor limitations for cultivation) and class 3 (more significant limitations for cultivation). The limitations of the class 2 and 3 soils are mainly due to stoniness, shallow depth, poor texture or chemistry [69].

The area was the site of the ancient Etruscan city of Veii, the richest city of the Etruscan League. It prospered until its defeat by Rome in 396 BC. It continued to be occupied under the Romans, but its eminence declined until the city was eventually abandoned [80]. From the 19th century, the site was studied by many scholars, including Gell, Nibby, Canina, Dennis, Stefani, Lanciani, Colini and Giglioli. After the Second World War, significant archaeological research in Veii was carried out by John Ward-Perkins of the British School at Rome [80]. More recently, the La Sapienza University of Rome carried out an extensive survey of the area as part of the "Veii Project". This includes analysis of a large archive of air photos and large scale geophysical (magnetometry) prospection. The magnetometry survey has covered almost the entire plateau and has revealed a dense network of buried streets and buildings [48]. This dataset has been used to compare with the SAR data.

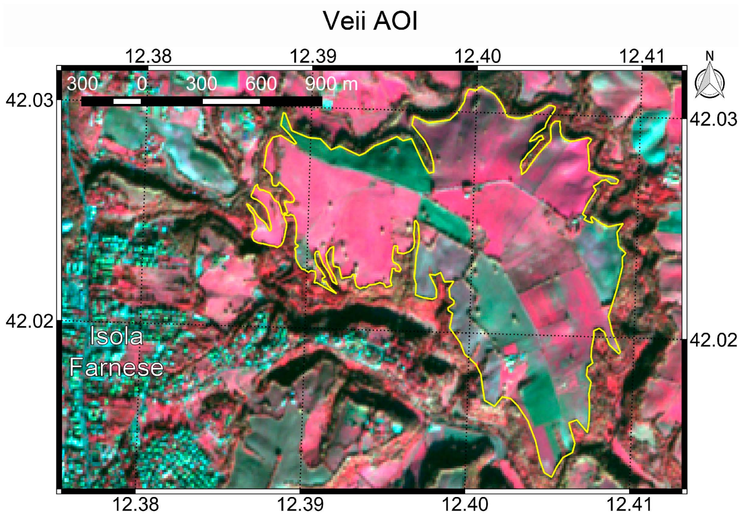

Figure 53. Sentinel-2 image of the Veii AOI (shown in yellow polygon), acquired on 28 December 2015. 10 m spatial resolution. Displayed as band 8 (NIR), band 4 (R) and band 3 (G) respectively as R, G and B. Pleiades data provided by the European Space Agency.

Analysis of the SAR data did not reveal any features which could be unequivocally associated with the presence of buried archaeological structures: neither in the filtered σ^0 backscatter, nor in the coherence time series. The coherence time series was characterized throughout by low coherence, which inhibited InSAR or SBAS DEM generation.

5. Discussion

Archaeological residues in the CSK data were clearly visible in 3 out of the 6 AOIs. The AOIs situated in the flat alluvial Tiber river valley and delta were perhaps more successful at revealing residues: in both the Portus and Salaria AOIs, features were clearly visible. Even in the Ostia AOI some very faint traces were found. The AOIs situated over the pyroclastic deposits of the Albano and Sabatino volcano districts were a little less successful at revealing residues and these were only found in 1 of the 3 (Prenestina). Moreover, in the case of Prenestina, most (if not all) of the anomalies appeared to be of a topographic nature. In most areas the soil types were of class 2 and 3, in most cases limited by stoniness, shallow depth, poor texture or chemistry, and in others by excess water, either in the form of stagnant water in the soil or possible flooding. Residues were found on all these soil types. They were also present on both irrigated and non-irrigated agricultural land.

No clear correlation could be found between residue contrast and PSMD. The residue of Road 497 in the Prenestina AOI was most apparent at a time of high water stress, but this was not the case for the other residues. However, the other residues that were not of an obvious topographic nature were situated over the alluvial Tiber plain, in irrigated fields. Over these areas PSMD may have been less relevant.

Not all archaeological structures documented in each area left residues in the SAR data. Mainly linear features, such as roads and canals, were evident. This is perhaps due to the easy recognition of the shape of such features. Many of the archaeological structures identified in the various surveys that took place in the AOIs were interpreted from scant surface remains. This is particularly the case for the survey reported in Quilici, [46] over the Prenestina AOI. These structures may no longer have a coherent shape that would allow easy interpretation on remotely sensed data.

Where archaeological residues were found, they were present in either the filtered σ^0 backscatter, the interferometric coherence (of 1 or 16 day temporal baseline), or the DEM (produced either by SBAS or InSAR). The sections below discuss the results of archaeological residue detection in each of the SAR data products.

5.1. Filtered σ^0 Backscatter

Multitemporal speckle filtering made a significant difference in the ability to distinguish archaeological residues in the σ^0 backscatter. Figure 54 illustrates this by comparing an image of σ^0 backscatter acquired on 20 December 2012 over the Northern Canal residue of the Portus AOI (Figure 54a), with the same image after having applied De Grandi speckle filtering using only 10 images (Figure 54b), and using all 75 images of the time series (Figure 54c). The filtering preserves the spatial resolution and the details in the image become increasingly clear the more images are used in the filtering. With 10 images, and particularly with 75 images, it is possible even to detect plough lines in the fields.

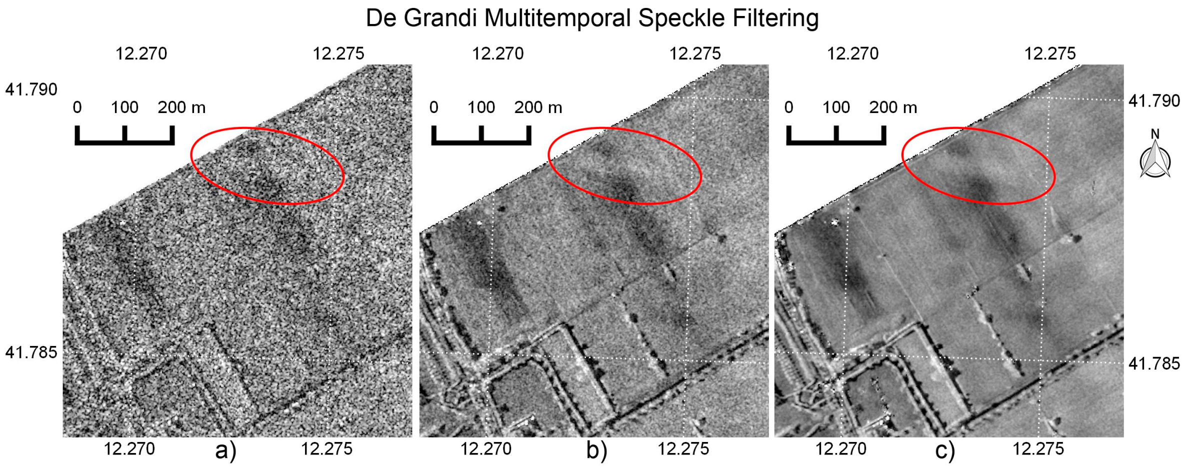

Figure 54. Examples of De Grandi multitemporal speckle filtering. (**a**) σ^0 backscatter image over Northern Canal in Portus AOI, acquired on 20 December 2012. Location of Northern Canal shown in red ellipse; (**b**) Same image as in (**a**) but De Grandi speckle filtered with 9 additional images. The Northern Canal is now easier to distinguish; (**c**) Same image as in (**a**) but De Grandi filtered with all 75 images in Stripmap time series. The Northern Canal appears a lot clearer. COSMO SkyMed images provided by the Italian Space Agency.

Residues were found in the images of filtered σ^0 backscatter both from higher and lower backscatter relative to surrounding areas. Each is described in the subsesctions below.

5.1.1. Filtered σ^0 Residues Due to High Relative Backscatter

Over both the Northern Canal in the Portus AOI and Road 497 in the Prenestina AOI, residues were distinguished by high backscatter.

In the case of the Northern Canal, the peak residue contrast was observed during times of very high coherence. Given the rapid temporal decorrelation in X-band SAR coherence over vegetated areas [60,61], it is unlikely that significant loose vegetation is present in areas where X-band coherence is high after a temporal baseline of 16 days. If coherence is high, it may be that the fields are occupied by bare soil, or rigid vegetation (e.g., dried stumps or crops fixed to poles). If either is the case, it is suggested that it may be properties of the soil (differences in moisture or composition) that reveal the buried structures. The photograph of the residue revealed no topographic (or any other) trace. No correlation between the contrast of the Northern Canal residue and PSMD was observed, but if the residue is situated in irrigated fields, it may be less likely to be affected by external moisture conditions.

The residue of Road 497 in the filtered σ^0 backscatter in the Prenestina AOI is also distinguished by high relative backscatter. In this case the coherence is always low. The UAV DEM reveals the presence of a very slight topographic valley corresponding to this feature. It may be that the high relative backscatter is a result of increased scattering from more abundant vegetation growth (positive crop mark), or an increased moisture presence. Such vegetation or moisture differences may be a result of subtle differences in water drainage in the valley. The valley itself is not visible on the ground, nor is any trace of the residue. The residue of Road 497 appears clearly at times of high PSMD, which is known to provoke the appearance of negative crop marks [1,5].

5.1.2. Filtered σ^0 Residues Due to Low Relative Backscatter

Over the built-up areas to the south of the Portus AOI, and over the AOI of the ancient Via Salaria, residues were distinguished by lower backscatter relative to surrounding areas. It is likely that these are both due to negative crop marks. In both cases low coherence is observed throughout the occurrence of residues, which may be a result of vegetation cover. The low backscatter may be indicative of shorter, stunted vegetation (smoother relative to the incident microwave signal), or it may be a result of a lower dielectric constant due to lower levels of moisture in parched vegetation, or shallower soil. These arguments are supported by the fact that both archaeological features causing the residues are objects made from construction material: confirmed by the magnetometer survey in the Portus AOI, and the negative crop mark in the optical image of the Via Salaria (probably due to basalt paving). No particular correlation was observed with PSMD, but this may again be expected if the residues in both AOIs are situated in irrigated fields.

The Portus AOI lies in the geologically flat area of the Tiber delta. Aside from on freely available topographic datasets from SRTM and ASTER GDEM, the topography of the Portus AOI was not measured at very high vertical accuracy. Moreover, the southern urban feature was not inspected, given access constraints. However, the nearby Northern Canal was possible to inspect, during which time no topographic trace was evident. When the area of the Via Salaria residue was inspected, it appeared flat, but the InSAR DEM revealed a clear low topographic anomaly over the Via Salaria itself. If this is due to stunted vegetation, it would support the interpretation of the low relative σ^0 backscatter residue as a negative crop mark.

5.2. Coherence

While the coherence was used throughout the AOIs to obtain additional surface information, the actual detection of residues on coherence images was limited to the Stripmap and Spotlight data over the Prenestina AOI. Here residues of lower relative coherence were identified that correspond to known archaeological structures. These residues are interpreted as positive crop marks, given that more abundant vegetation is likely to reduce coherence [61,62]. In most cases the residues were in topographic valleys, and it is likely that the coherence anomalies are a result of topography induced moisture and soil differences resulting in differential vegetation growth. If this is the case with the residue of Road 497, it would suggest that even very subtle variations in the topography, not visible to the naked eye at the surface, are sufficient to cause coherence residues. Over the ancient Via Salaria, a topographic anomaly was detected, but this was not identified in any of the coherence images. However, low coherence was observed throughout most of the InSAR time series in this area, and the few occasions when coherence was not completely lost did not coincided with the appearance of σ^0 residues. It is likely therefore that the conditions for differential crop growth were not present when they may have been detected in the coherence.

The coherence residues occurred at times of peak PSMD (in dry periods). The peak residue occurred in a coherence image with a 16 day temporal baseline (between 9 and 25 July 2010). However, this happened to span the time of peak PSMD in the time series and in general the 1 day coherences yielded higher contrast residues.

5.3. DEM

The SBAS processing was successful only over 2 of the 6 AOIs using both Stripmap (Prenestina and Salaria) and Spotlight (Prenestina) CSK data. However, over Salaria only a very noisy result with one interferometric pair was possible. In both AOIs topographic anomalies corresponding to locations of known archaeological structures were detected. In the case of Prenestina, these were visible on the ground as valleys of varying width, but in the case of Salaria, there was no topographic evidence on the ground. However, the area was not inspected at the same time as the acquisitions of the images with which the DEM was created. There may have been differential vegetation growth, in the form of a negative crop mark, sufficient to be detected on a DEM derived from Stripmap data, even if not on the σ^0 imagery. In the case of Prenestina, the topographical anomalies seemed permanent.

Repeat pass SAR interferometry may not be the most efficient technique for DEM generation over vegetated areas. Nonetheless, the results presented here show that it can in some cases be applied successfully. This may complement information provided by backscatter intensity and coherence derived from the same data. DEMs produced from the TanDEM-X mission have been used for the detection of palaeolandscape features [81]. TanDEM-X takes advantage of two satellites flying in close formation, thus minimising temporal decorrelation [82]. The vertical accuracy of spaceborne InSAR may not match that of airborne systems, but it may be sufficient to identify archaeological structures. Even if these are evident on the ground, the synoptic view enables a much better distinction between natural and artificially created topographic relief (such as that created by an ancient road).

6. Conclusions

In vegetated areas around the city of Rome, surface residues over buried archaeological features clearly appear in imagery derived from both the intensity and the phase of SAR data. This imagery includes multitemporal speckle filtered σ^0 backscatter, interferometric coherence, and DEMs derived from InSAR and SBAS. The clarity of residues in each of these types of SAR data often differs between features and over time. The application of both intensity and interferometric SAR processing therefore contributes to increasing the probability of detecting traces of buried archaeological structures. It also combines to provide a better understanding of their underlying cause. Comparisons between σ^0 backscatter, coherence and DEMs have aided interpretation of trace features as manifestations of positive and negative crop marks, soil marks and topographic residues.

A large time series of SAR data greatly improves the quality of information and potential for extracting small scale features, such as buried structures. With such a time series the speckle in images of backscatter intensity can be greatly reduced while preserving spatial resolution if techniques such as De Grandi filtering are applied [49]. The ability to derive topographic information using repeat pass interferometry is significantly limited in vegetated areas by temporal decorrelation. However, with a large time series, techniques such as SBAS can in some cases overcome such limitations. The interferometric coherence can be used to derive some information on surface characteristics, such as the fallow or vegetated state of a field. With a time series, such information can be derived with higher confidence if the measurements can be correlated with a possible crop cycle, or vegetation growth. Archaeological residues can be notoriously ephemeral, and their appearance depends on many factors, which are often very site specific. The higher the frequency of acquisition, the more likely an archaeological residue can be detected when it appears.

In practice a large time series may be difficult to acquire for archaeological analysis. Moreover, the processing techniques described are complex and time consuming, especially SBAS. However, the current trend in Earth Observation (EO) is characterized by an unprecedented rate of increase in the volume, variety and velocity of remotely sensed data, now coined as "Big Data". This is becoming progressively available to users as access restrictions are lifted. Developments in EO closely accompany advances in IT, and complex data processing is increasingly automatized with the aid of cloud computing and big data analytics.

SAR data analysis could in the future become a routine and cost effective technique for extracting high quality information on buried archaeological structures. It is unlikely to replace existing, more conventional methods for archaeological survey, such as active (LiDAR) and passive optical remote sensing and geophysical survey. However, it may complement these by providing unique information. The identification of archaeological structures is of paramount importance for their documentation, preservation and valorisation.

Supplementary Materials: The following are available online at www.mdpi.com/2072-4292/9/2/118/s1, Table S1: Full list of COSMO SkyMed data used for the analysis.

Acknowledgments: The SAR data was provided by the Italian Space Agency (ASI): 25 Stripmap and 8 Spotlight images were procured for the ASI World Heritage Monitoring by Remote Sensing (WHERE) project, an experimental component of which included research on the use of SAR for prospection of archaeological vegetation and soil residues. This component constitutes the research reported in this paper. A further 52 Stripmap and 19 Spotlight CSK images were provided by ASI for an advanced SAR remote sensing training event provided to the Italian Ministry of Defense and ASI, and hosted by the European Space Agency (ESA). The two week course took place from 9 to 20 November 2015. The processing reported in this paper constituted a part of the practical exercises of the course. The optical satellite data (Pleiades, Kompsat-2 and Sentinel-2) was provided by the European Space Agency (ESA). The software used for the processing included the SARscape software, version 5.2. Much support in the SAR data processing was provided by the team of Sarmap SA. The UAV flight, which took place on 6 October 2015 over parts of the Prenestina AOI, was carried out by a team from the National Research Council of Italy (CNR), Institute of Methodologies for Environmental Analysis (IMAA).

Conflicts of Interest: The author declares no conflict of interest.

References

1. Jones, R.; Evans, R. Soil and crop marks in the recognition of archaeological sites by air photography. In *Aerial Reconnaissance for Archaeology*; Archaeology Data Service: York, UK, 1975; pp. 1–11.
2. Stanjek, H.; Fassbinder, J. Soil aspects affecting archaeological details in aerial photographs. *Archaeol. Prospect.* **1995**, *2*, 91–102.
3. Wilson, D.R. *Air Photo Interpretation for Archaeologists*; Tempus Publishing: Stroud, UK, 2000.
4. Lasaponara, R.; Masini, N. *Satellite Remote Sensing: A New Tool for Archaeology*; Springer Science & Business Media: New York, NY, USA, 2012; Volume 16.
5. Evans, R.; Jones, R. Crop marks and soils at two archaeological sites in britain. *J. Archaeol. Sci.* **1977**, *4*, 63–76. [CrossRef]
6. Lasaponara, R.; Masini, N. Remote sensing in archaeology: From visual data interpretation to digital data manipulation. In *Satellite Remote Sensing*; Springer: Berlin/Heidelberg, Germany, 2012; pp. 3–16.
7. Kaimaris, D.; Patias, P.; Tsakiri, M. Best period for high spatial resolution satellite images for the detection of marks of buried structures. *Egypt. J. Remote Sens. Space Sci.* **2012**, *15*, 9–18. [CrossRef]
8. Agapiou, A.; Alexakis, D.D.; Hadjimitsis, D.G. Spectral sensitivity of alos, aster, ikonos, landsat and spot satellite imagery intended for the detection of archaeological crop marks. *Int. J. Digit. Earth* **2014**, *7*, 351–372. [CrossRef]
9. Agapiou, A.; Hadjimitsis, D.G.; Sarris, A.; Georgopoulos, A.; Alexakis, D.D. Optimum temporal and spectral window for monitoring crop marks over archaeological remains in the mediterranean region. *J. Archaeol. Sci.* **2013**, *40*, 1479–1492. [CrossRef]
10. Rączkowski, W. Cropmarks 2011 in poland—Is there a need for further discussion? *AARGnews* **2011**, *43*, 37–42.
11. Crawford, O.G.S. Air survey and archaeology. *Geogr. J.* **1923**, *61*, 342–360. [CrossRef]
12. Knipling, E.B. Physical and physiological basis for the reflectance of visible and near-infrared radiation from vegetation. *Remote Sens. Environ.* **1970**, *1*, 155–159. [CrossRef]
13. Gates, D.M. *Biophysical Ecology*; Springer: New York, NY, USA, 1980; p. 614.
14. Myneni, R.B.; Hall, F.G.; Sellers, P.J.; Marshak, A.L. The interpretation of spectral vegetation indexes. *IEEE Trans. Geosci. Remote Sens.* **1995**, *33*, 481–486. [CrossRef]
15. Lasaponara, R.; Masini, N. Detection of archaeological crop marks by using satellite quickbird multispectral imagery. *J. Archaeol. Sci.* **2007**, *34*, 214–221. [CrossRef]

16. Agapiou, A.; Alexakis, D.D.; Sarris, A.; Hadjimitsis, D.G. Orthogonal equations of multi-spectral satellite imagery for the identification of un-excavated archaeological sites. *Remote Sens.* **2013**, *5*, 6560–6586. [CrossRef]
17. Cavalli, R.M.; Colosi, F.; Palombo, A.; Pignatti, S.; Poscolieri, M. Remote hyperspectral imagery as a support to archaeological prospection. *J. Cult. Herit.* **2007**, *8*, 272–283. [CrossRef]
18. Doneus, M.; Verhoeven, G.; Atzberger, C.; Wess, M.; Ruš, M. New ways to extract archaeological information from hyperspectral pixels. *J. Archaeol. Sci.* **2014**, *52*, 84–96. [CrossRef]
19. Atzberger, C.; Wess, M.; Doneus, M.; Verhoeven, G. Arctis—A Matlab® Toolbox for archaeological imaging spectroscopy. *Remote Sens.* **2014**, *6*, 8617–8638. [CrossRef]
20. Ben-Dor, E.; Portugali, J.; Kochavi, M.; Shimoni, M.; Vinitzky, L. Airborne thermal video radiometry and excavation planning at Tel Leviah, Golan Heights, Israel. *J. Field Archaeol.* **2013**, *26*, 117–127. [CrossRef]
21. McManus, K.; Donoghue, D. Airborne Thermography of the Vegetation-Soil Interface for Detecting Shallow Ground Disturbance. Space Applications for Heritage Conservation. In Proceedings of the EGS XXVII General Assembly, Nice, France, 21–26 April 2002; p. 31.
22. Verhoeven, G.J.; Schmitt, K.D. An attempt to push back frontiers–digital near-ultraviolet aerial archaeology. *J. Archaeol. Sci.* **2010**, *37*, 833–845. [CrossRef]
23. Ulaby, T.; Moore, K.; Fung, K. *Microwave Remote Sensing. Volume II: Radar Remote Sensing and Surface Scattering and Emission Theory*; Addison Wesley: New York, NY, USA, 1982; Volume 2.
24. McCauley, J.F.; Schaber, G.G.; Breed, C.S.; Grolier, M.J.; Haynes, C.V.; Issawi, B.; Elachi, C.; Blom, R. Subsurface valleys and geoarcheology of the eastern sahara revealed by shuttle radar. *Science* **1982**, *218*, 1004–1020. [CrossRef] [PubMed]
25. Schaber, G.G.; McCauley, J.F.; Breed, C.S.; Olhoeft, G.R. Shuttle imaging radar: Physical controls on signal penetration and subsurface scattenng in the eastern sahara. *IEEE Trans. Geosci. Remote Sens.* **1986**, 603–623. [CrossRef]
26. Paillou, P.; Grandjean, G.; Baghdadi, N.; Heggy, E.; August-Bernex, T.; Achache, J. Subsurface imaging in south-central egypt using low-frequency radar: Bir safsaf revisited. *IEEE Trans. Geosci. Remote Sens.* **2003**, *41*, 1672–1684. [CrossRef]
27. Morrison, K. Mapping subsurface archaeology with sar. *Archaeol. Prospect.* **2013**, *20*, 149–160. [CrossRef]
28. Gaber, A.; Koch, M.; Griesh, M.H.; Sato, M.; El-Baz, F. Near-surface imaging of a buried foundation in the western desert, egypt, using space-borne and ground penetrating radar. *J. Archaeol. Sci.* **2013**, *40*, 1946–1955. [CrossRef]
29. Stewart, C.; Lasaponara, R.; Schiavon, G. Alos palsar analysis of the archaeological site of pelusium. *Archaeol. Prospect.* **2013**, *20*, 109–116. [CrossRef]
30. Dubois, P.C.; Van Zyl, J.; Engman, T. Measuring soil moisture with imaging radars. *IEEE Trans. Geosci. Remote Sens.* **1995**, *33*, 915–926. [CrossRef]
31. Rosen, P.A.; Hensley, S.; Joughin, I.R.; Li, F.K.; Madsen, S.N.; Rodriguez, E.; Goldstein, R.M. Synthetic Aperture Radar interferometry. *Proc. IEEE* **2000**, *88*, 333–382. [CrossRef]
32. Lanari, R.; Casu, F.; Manzo, M.; Zeni, G.; Berardino, P.; Manunta, M.; Pepe, A. An overview of the small baseline subset algorithm: A dinsar technique for surface deformation analysis. *Pure Appl. Geophys.* **2007**, *164*, 637–661. [CrossRef]
33. Moore, E.; Freeman, A. The Application of Microwave Scattering Mechanism to the Study of Early Ankorean Water Management. Paper Read at European Association of Southeast Asian Archaeologists. In Proceedings of the 6th International Conference, Leiden, The Netherlands, 2–6 September 1996; pp. 1–13.
34. Moore, E.; Freeman, T.; Hensley, S. Spaceborne and airborne radar at Angkor: Introducing new technology to the ancient site. In *Remote Sensing in Archaeology*; Springer: Berlin/Heidelberg, Germany, 2007; pp. 185–216.
35. Sheets, P.; Sever, T.L. Creating and perpetuating social memory across the ancient Costa Rican Landscape. In *Remote Sensing in Archaeology*; Springer: Berlin/Heidelberg, Germany, 2006; pp. 161–184.
36. Stewart, C.; Lasaponara, R.; Schiavon, G. Multi-frequency, polarimetric SAR analysis for archaeological prospection. *Int. J. Appl. Earth Observ. Geoinform.* **2014**, *28*, 211–219. [CrossRef]
37. Stewart, C.; Di Iorio, A.; Schiavon, G. Analysis of the utility of COSMO SkyMed stripmap to detect buried archaeological features in the region of Rome. In Proceedings of the 4th EARSeL Workshop on Cultural and Natural Heritage, Matera, Italy, 6–7 June 2013; Lasaponara, R., Masini, N., Biscione, M., Hernandez, M., Eds.; European Association of Remote Sensing Laboratories (EARSeL): Matera, Italy, 2013; pp. 203–212.

38. Chen, F.; Masini, N.; Yang, R.; Milillo, P.; Feng, D.; Lasaponara, R. A space view of radar archaeological marks: First applications of COSMO-SkyMed X-band data. *Remote Sens.* **2015**, *7*, 24–50. [CrossRef]
39. Sever, T.L.; Irwin, D.E. Landscape archaeology: Remote-sensing investigation of the ancient maya in the peten rainforest of Northern Guatemala. *Anc. Mesoam.* **2003**, *14*, 113–122. [CrossRef]
40. Comer, D.C.; Blom, R.G. Detection and identification of archaeological sites and features using Synthetic Aperture Radar (SAR) data collected from airborne platforms. In *Remote Sensing in Archaeology*; Springer: Berlin/Heidelberg, Germany, 2006; pp. 103–136.
41. Funiciello, R.; Heiken, G.; De Rita, D. *I Sette Colli: Guida Geologica a una Roma Mai Vista*; Raffaello Cortina: Milano, Italy, 2006.
42. Centro Funzionale Regionale. Available online: http://www.idrografico.roma.it/ (accessed on 20 October 2016).
43. Keay, S.; Millett, M.; Paroli, L.; Strutt, K. *Portus: An Archaeological Survey of the Port of Imperial Rome*; British School at Rome: London, UK, 2005; Volume 15, p. 360.
44. Becker, H. Prospecting in Ostia Antica (Italy) and the Discovery of the Basilica of Constantinus I. In 1996. *ICOMOS Hefte Dtsch. Natl.* **2015**, *33*, 139–143.
45. Mols, S. Mapping the via appia. *Forma Urbis* **2014**, *XIX*, 4.
46. Quilici, L. *Collatia*; De Luca Editore: Rome, Italy, 1974; Volume Regio 1, p. 938.
47. Quilici, L.; Gigli, S.Q. *Crustumerium*; Consiglio Nazionale Delle Ricerche, Centro di Studio per L'archeologia Etrusco-Italica: Rome, Italy, 1980; Volume 3.
48. Campana, S. *Filling Gaps in Space and Time at Veii. 'Emptyscapes' Project*; University of Texas Press: Auxtin, TX, USA, 2016.
49. De Grandi, G.; Leysen, M.; Lee, J.; Schuler, D. In Radar reflectivity estimation using multiple sar scenes of the same target: Technique and applications. In Proceedings of the 1997 IEEE International Geoscience and Remote Sensing, Remote Sensing—A Scientific Vision for Sustainable Development (IGARSS'97), Singapore, 3–8 August 1997; pp. 1047–1050.
50. Stewart, C.; Montanaro, R.; Sala, M.; Riccardi, P. Feature extraction in the north sinai desert using spaceborne Synthetic Aperture Radar: Potential archaeological applications. *Remote Sens.* **2016**, *8*, 825. [CrossRef]
51. Ferretti, A.; Monti-Guarnieri, A.; Prati, C.; Rocca, F.; Massonnet, D. *Insar Principles: Guidelines for SAR Interferometry Processing and Interpretation*; ESA Publications Division, ESTEC: Noordwijk, The Netherlands, 2007; Volume 19.
52. Woodhouse, I.H. *Introduction to Microwave Remote Sensing*; CRC Press: Boca Raton, FL, USA, 2005; p. 370.
53. Berardino, P.; Fornaro, G.; Lanari, R.; Sansosti, E. A new algorithm for surface deformation monitoring based on small baseline differential SAR interferograms. *IEEE Trans. Geosci. Remote Sens.* **2002**, *40*, 2375–2383. [CrossRef]
54. Chen, J.X. Geographic information systems. *Comput. Sci. Eng.* **2010**, *12*, 8–9. [CrossRef]
55. Inglada, J.; Mercier, G. A new statistical similarity measure for change detection in multitemporal SAR images and its extension to multiscale change analysis. *IEEE Trans. Geosci. Remote Sens.* **2007**, *45*, 1432–1445. [CrossRef]
56. Pathe, C.; Wagner, W.; Sabel, D.; Doubkova, M.; Basara, J.B. Using envisat asar global mode data for surface soil moisture retrieval over oklahoma, USA. *IEEE Trans. Geosci. Remote Sens.* **2009**, *47*, 468–480. [CrossRef]
57. Monteith, J.; Unsworth, M. *Principles of Environmental Physics*; Academic Press: New York, NY, USA, 2007.
58. Bartalis, Z.; Wagner, W.; Naeimi, V.; Hasenauer, S.; Scipal, K.; Bonekamp, H.; Figa, J.; Anderson, C. Initial soil moisture retrievals from the METOP—A Advanced Scatterometer (ASCAT). *Geophys. Res. Lett.* **2007**, *34*. [CrossRef]
59. Kerr, Y.H.; Waldteufel, P.; Wigneron, J.-P.; Martinuzzi, J.; Font, J.; Berger, M. Soil moisture retrieval from space: The Soil Moisture and Ocean Salinity (SMOS) mission. *IEEE Trans. Geosci. Remote Sens.* **2001**, *39*, 1729–1735. [CrossRef]
60. Zalite, K.; Antropov, O.; Praks, J.; Voormansik, K.; Noorma, M. Monitoring of agricultural grasslands with time series of X-band repeat-pass interferometric SAR. *IEEE J. Sel. Top. Appl. Earth Observ. Remote Sens.* **2016**, *9*, 3687–3697. [CrossRef]
61. Zalite, K.; Voormansik, K.; Praks, J.; Antropov, O.; Noorma, M. Towards detecting mowing of agricultural grasslands from multi-temporal COSMO-SkyMed data. In Proceedings of the 2014 IEEE Geoscience and Remote Sensing Symposium, Quebec City, QC, Canada, 13–18 July 2014; pp. 5076–5079.

62. Engdahl, M.E.; Borgeaud, M.; Rast, M. The use of ERS-1/2 Tandem interferometric coherence in the estimation of agricultural crop heights. *IEEE Trans. Geosci. Remote Sens.* **2001**, *39*, 1799–1806. [CrossRef]
63. Modigliani, D. Carta geolitologica del territorio comunale. In *Piano Regolatore Generale*; Comune di Roma: Rome, Italy, 2008.
64. Modigliani, D. Carta dell'uso del suolo e delle fisonomie vegetazionali del territorio comunale. In *Piano Regolatore Generale*; Comune di Roma: Rome, Italy, 2008.
65. Keay, S.J.; Parcak, S.H.; Strutt, K.D. High resolution space and ground-based remote sensing and implications for landscape archaeology: The case from Portus, Italy. *J. Archaeol. Sci.* **2014**, *52*, 277–292. [CrossRef]
66. Lanciani, R. *Ricerche Topografiche Sulla Città di Porto*; Annali Dell'istituto di Corrispondenza Archeologica: Rome, Italy, 1868; Volume 51.
67. Lugli, G.; Filibeck, G. *IL Porto di Roma Imperialee L'agro Portuense*; Officine Dell'istituto Italiano D'Arti Grafiche: Bergamo, Italy, 1935.
68. Testaguzza, O. *Portus: Illustrazione dei Porti di Claudio e Traiano e Della Città di Porto a Fiumicino*; Julia Editrice: Rome, Italy, 1970.
69. Modigliani, D. Carta agropedologica del territorio comunale. In *Piano Regolatore Generale*; Comune di Roma: Rome, Italy, 2008.
70. Bellotti, P.; Calderoni, G.; Di Rita, F.; D'Orefice, M.; D'amico, C.; Esu, D.; Magri, D.; Martinez, M.P.; Tortora, P.; Valeri, P. The Tiber River Delta Plain (Central Italy): Coastal Evolution and Implications for the Ancient Ostia Roman Settlement. *Holocene* **2011**, *21*, 1105–1116. [CrossRef]
71. Meiggs, R. *Roman Ostia*, 2nd ed.; Oxford University Press: Oxford, UK, 1973.
72. Linck, R.; Busche, T.; Buckreuss, S. Possibilities of Terrasar-X data for the prospection of archaeological sites by SAR. In Proceedings of the 5th TerraSAR-X/4th TanDEM-X Science Team Meeting, Oberpfaffenhofen, Germany, 10–14 June 2013; German Aerospace Center (DLR): Oberpfaffenhofen, Germany, 2013; p. 4.
73. Modigliani, D. Carta delle serie di vegetazione del territorio comunale. In *Piano Regolatore Generale*; Comune di Roma: Rome, Italy, 2008.
74. Della Portella, I.; Sartorio, G.P.; Ventre, F. *The Appian Way: From Its Foundation to the Middle Ages*; Getty Publications: Los Angeles, CA, USA, 2004.
75. De Franceschini, M. *Ville Dell'agro Romano*; L'erma di Bretschneider: Rome, Italy, 2005; p. 564.
76. Rosa, P. *Carta Topografica del Lazio*; Archaeological Chart of Lazio, at a Scale of 1:20,000; Soprintendenza di Roma: Rome, Italy, 1870.
77. Wiseman, T. Roman republican road building. In *Papers of the British School at Rome*; British School at Rome: Rome, Italy, 1970; Volume 38, p. 30.
78. Hyppönen, P. *Salaria via Usque ad Lapidem XVIII, a Reconstruction of the Ancient Road Line between Porta Collina and the 18th Milestone of the Road*; University of Oulu: Oulu, Finland, 2014.
79. Quilici, L. Evoluzione della tecnica stradale Nell'Italia centrale. In *Atlante Tematico di Topografia Antica 1. Tecnica Stradale Romana*; L'Erma di Bretschneider: Rome, Italy, 1992; Volume 13.
80. Ward-Perkins, J.B. Veii: The historical topography of the ancient city. In *Papers of the British School at Rome*; British School at Rome: Rome, Italy, 1961; Volume 29, pp. 1–119.
81. Erasmi, S.; Rosenbauer, R.; Buchbach, R.; Busche, T.; Rutishauser, S. Evaluating the quality and accuracy of Tandem-X digital elevation models at archaeological sites in the Cilician Plain, Turkey. *Remote Sens.* **2014**, *6*, 9475–9493. [CrossRef]
82. Zink, M.; Bachmann, M.; Brautigam, B.; Fritz, T.; Hajnsek, I.; Moreira, A.; Wessel, B.; Krieger, G. Tandem-X: The new global dem takes shape. *IEEE Geosci. Remote Sens. Mag.* **2014**, *2*, 8–23. [CrossRef]